DOCTORAL THESIS

Constructing Poly(Ionic Liquid)s-Based Solid State Electrolytes and Application in Lithium Metal Batteries

Jiajia Li

Energy Engineering

LULEÅ UNIVERSITY OF TECHNOLOGY

Doctoral Thesis

Constructing Poly(Ionic Liquid)s-Based Solid State Electrolytes and Application in Lithium Metal Batteries

Jiajia Li

Division of Energy Science
Department of Engineering Sciences and Mathematics
Luleå University of Technology

Luleå 2025

Acknowledgment

This work was conducted within M-ERA.NET 3 with support from European Union's Horizon 2020 research and innovation programme under grant agreement No. 958174, Vinnova (Swedish Governmental Agency for Innovation Systems), EU/Interreg Nord, Region Norrbotten in Sweden (SolBat, 304-16169-2019), Swedish Energy Agency, and STINT (CH2019-8287). The research was carried out at the Division of Energy Science, Department of Engineering Sciences and Mathematics, Luleå University of Technology (LTU) during 2020-2025.

Firstly, I would like to express my heartfelt gratitude to my principal supervisor, Prof. Xiaoyan Ji, for her meticulous guidance and unwavering support. She invested a lot of time and effort into every aspect of my research, ranging from topic selection to experimental arrangement and manuscript revision. Additionally, I extend my sincere thanks to my co-supervisors, Prof. Marcus Öhman from LTU and Prof. Haitao Zhang from the Institute of Process Engineering (IPE), Chinese Academy of Sciences (CAS), for their valuable insights and for creating optimal experimental conditions for my work.

Secondly, I extend my gratitude to all my friends and colleagues at LTU and IPE, whose support and valuable suggestions have not only enriched my work but also brought me immense happiness throughout this journey.

Lastly, I must emphasize my profound appreciation to my family for their unwavering support, which made it possible for me to pursue my doctoral studies at LTU. Their encouragement and belief in me have been the driving force behind my achievements, and I am forever indebted to them.

Abstract

Lithium metal batteries (LMBs) are attracting attention for their potential to enhance energy density while offering safety over conventional Li-ion batteries (LIBs), yet face critical challenges like dendrite growth and short cycling life. Developing compatible and effective solid-state electrolytes (SSEs) has been proposed as one effective strategy to address the challenge.

SSEs are typically classified into inorganic solid electrolytes (ISEs), solid polymer electrolytes (SPEs), and solid composite electrolytes (SCEs), all of which exhibit inherent limitations hindering their ideal performance. The SSEs using polymer are promising in further development owing to the capabilities of the polymer in facilitating Li^+ transport and compatibility with existing membrane manufacturing processes. However, the current polymers in LMBs suffer from poor high-voltage stability, making it challenging to achieve long cycle life. Poly(ionic liquid)s (polyILs), a new type of polymer that incorporates the properties of ionic liquids (ILs), including wide electrochemical stability window (ESW) and high ionic conductivity, into polymer frameworks, offer a promising alternative to the traditional polymers in SSEs.

This thesis aims to develop polyIL-based SSEs with enhanced ionic conductivity, a wide ESW, a high lithium transference number (t_{Li^+}), reduced electrodes/electrolyte interface resistance, and suppression of lithium dendrites growth, ultimately enabling LMBs with extended cycle life. These objectives are achieved by tuning the constituents of the polyIL-based SSEs. The specific achievements of this thesis are as follows:

1. The application of ILs in SSEs and their effects on LMB performance were reviewed and summarized. The analysis highlighted that ILs can improve ionic conductivity, broaden the ESW of electrolytes, and enhance interface contact between the electrode and electrolyte. Considering the overall performance of ILs, including high ionic conductivity, a wide ESW, and cost-effectiveness, EMIMTFSI was selected for subsequent experiments.

2. Three F-based Li-salts were selected to prepare SSEs using poly(ethylene oxide) host and polyimide substrate. The investigation focused on the impact of F content and chemical structures (F-connecting bonds) of these Li-salts on the cell performance and uncovering the formation process of LiF in the solid electrolyte interphase (SEI). The results revealed that the F-connecting bond plays a more significant role than the F

element content, resulting in slightly better cell performance using LiPFSI than LiTFSI and substantially better performance than LiFSI. The preferential breakage of bonds in LiPFSI was found to be related to its position to the Li anode. Consequently, the LiPFSI reduction mechanism was proposed.

3. Using the template method, a polyIL-based SCE was synthesized with boron nitride (BN) nanosheets as inert inorganic fillers. BN was chosen due to its high specific surface area and porous structure. An optimal BN content of 1.6 wt% was found to increase the amorphous regions of the polyIL, facilitating Li^+ migration, and enhancing both t_{Li^+} and ionic conductivity. The Li//$LiFePO_4$ cell assembled with the optimized SCE delivered a stable specific capacity of up to 152 mA h g^{-1} after 300 cycles.

4. A concentration gradient polyIL-based SCE (GSCE) was synthesized via natural sedimentation and photopolymerization to simultaneously meet the distinct requirements of both the cathode and the lithium metal anode. The concentration of active inorganic filler was optimized, with 5 wt% as the optimal content. Compared to the uniform SCE, the GSCE demonstrated a higher t_{Li^+} and improved ionic conductivity. As a result, the Li/GCSE-5/LMFP cell operated at a cut-off potential of 4.3 V and exhibited a long cycle life.

5. A polyIL-based SSE was developed by combining a polyIL material host with a modified cellulose acetate (CA)-polyIL substrate to enrich diverse functional groups. This design effectively mitigated the non-uniform filler distribution within the polymer host while maintaining high mechanical strength and facilitating the Li^+ migration. Additionally, the use of the same polyIL-based material as a cathode binder significantly improved the electrode-SPE interfacial compatibility. As a result, the developed LMB demonstrated stable operation at a high cut-off potential of 4.8 V and an extended cycle life.

List of publications included in this thesis

I. **J. Li**, F. Li, L. Zhang, H. Zhang, U. Lassi, X. Ji. Recent applications of ionic liquids in quasi-solid-state lithium metal batteries. ***Green Chemical Engineering***, 2021, 2, 253.

J. Li, the primary author, conducted the literature review, analyzed the results, and wrote the manuscript, while the co-authors contributed to the editing process.

II. **J. Li**, L. Yang, H. Zhang, X. Ji. Self-healing composite solid electrolytes with enhanced Li^+ transport and mechanical properties for safe lithium metal batteries. ***Chemical Engineering Journal***, 2022, 438, 135418.

J. Li conducted the literature review, experiments, data analysis, and manuscript preparation, while co-authors contributed to discussions and editing, and performed TEM, SEM, AFM, XPS, and SAXS experiments.

III. **J. Li**, H. Hu, W. Fang, J. Ding, D. Yuan, S. Luo, H. Zhang, X. Ji. Impact of fluorine-based lithium salts on SEI for all-solid-state PEO-based lithium metal batteries. ***Advanced Functional Materials***, 2023, 33, 2303718.

J. Li conducted the literature review, experiments, data analysis, and manuscript preparation, while co-authors contributed to discussions and editing, and performed ^{7}Li NMR, SEM, XPS, ToF-SIMS, and simulations.

IV. **J. Li**, J. Zhu, H. Hu, H. Zhang, X. Ji, S. Zhang. Gravity field induced composite solid electrolytes enabling enhanced Li^+ transport kinetics of lithium metal battery. ***Chemical Engineering Journal***, 2024, 484, 149781.

J. Li did the literature review, drew up the experiment plan, executed the experiments, evaluated the outcomes, and wrote the manuscript. The co-authors performed rheological test, coefficients of thermal expansion measurements, and conducted ^{7}Li NMR, SEM, TEM, XPS, ToF-SIMS, and simulations.

V. **J. Li**, H. Hu, J. Zhu, X. Ma, Y. Hu, H. Zhang, M. Liu, S. Zhang, X. Ji. Solid polymer electrolyte with compatibility cathode-electrolyte interfacial design enabling lithium metal batteries operation at 4.8 V with long cycle life. *Submitted to Advanced Materials.*

J. Li did the literature review, designed the experiments, performed the research, and wrote the manuscript. The co-authors contributed to discussions and manuscript editing, and performed SEM, EDS, TEM, XPS, in-situ Raman, and simulations.

List of publications not included in this thesis

I. L. Hu, X. Yang, Y. Chen, L. Wang, **J. Li**, Y. Tang, H. Zhang. Facile construction of hierarchical $TiNb_2O_7$/rGO nanoflower with robust charge storage properties for Li ion batteries via an esterification reaction. ***Frontiers in Energy Research***, 2021, 9, 794527.

II. H. Da, W. Fang, J. Zhu, J. Li, S. Pan, **J. Li**, J. Huang, H. Zhang, S. Zhang. Superior rate capability of small regenerated graphite particles induced by homogenously distributed current density derived from cracks and intrinsic defects. ***Small***, 2023, 19, 2304060.

III. H. Hu, **J. Li**, X. Ji. Confining ionic liquids in developing quasi-solid-state electrolytes for lithium metal batteries. ***Chemistry—A European Journal***, 2024, 30, e202302826.

IV. H. Hu, **J. Li**, Y. Wu, W. Fang, H. Zhang, X. Ji. Revealing the role and working mechanism of confined ionic liquids in solid polymer composite electrolytes. ***Journal of Energy Chemistry***, 2024, 99, 110.

Table of contents

1. Introduction

1.1 Background

At the end of the 19th century, a visionary assertion was made by a later Nobel laureate Friedrich Wilhelm Ostwald that the biggest challenge of his time, namely, securing affordable and clean energy, could be resolved only by electrochemistry.[1] History rhymes, at the end of the 20th century, another Nobel laureate, Richard Errett Smalley, advocated a list entitled ''Top Ten Problems of Humanity for Next 50 Years'', in which the need for cheap and clean energy has been ranked number one.[2, 3] To tackle the grand challenge in the energy sector, electrochemical energy conversion and storage have played and will continue to play a critical role.[4]

Among the numerous types of electrochemical energy conversion and storage devices (batteries, fuel cells, supercapacitors, etc.), Li-ion batteries (LIBs) have achieved great success in the history of electrochemistry because of the high energy density, long cycle life, and low self-discharge.[5] The emergence of LIBs has revolutionized portable electronics and the daily life of the contemporary population.[6] However, with the best technology of today, the gravimetric energy density of LIBs (around 300 Wh kg^{-1})[7] is approaching their theoretical limit, making it almost impossible to further increase to satisfy the demands of today's energy-storage applications, especially in the electric vehicles (EVs) and power grid.

Lithium metal with low reduction potential (-3.04 V vs. standard hydrogen electrode) and high theoretical specific capacity (3860 mAh g^{-1}),[8] is considered a promising substitute for the graphite anode (0.05 V and 372 mAh g^{-1}) in LIBs to develop lithium metal batteries (LMBs). However, simply replacing the graphite anode with lithium metal is not feasible, as the low reduction potential of lithium metal can cause a series of problems when using the same liquid organic electrolytes as in LIBs, such as persistent side reactions, overpotential, and severe lithium dendrites growth. Additionally, such liquid organic electrolytes typically have a low operating potential ($\leq$ 4.0 V vs. Li/Li^+), limiting the possibility of enhancing the energy density via pairing with high-voltage cathodes, like $LiMn_xFe_{1-x}PO_4$ (LMFP $\geq$ 4.1 V vs. Li/Li^+), $LiCoO_2$ (LCO $\geq$ 4.2 V vs. Li/Li^+), and $LiNi_xCo_yMn_{1-x-y}O_2$ (NCM $\geq$ 4.2 V vs. Li/Li^+). Moreover, the leakage of these electrolytes during assembly and operation poses significant safety and hazard risks.[9]

To address the challenges associated with the lithium metal anode and enable LMBs to

operate with high-voltage cathodes and high safety, solid-state electrolytes (SSEs) are proposed as alternatives to liquid organic electrolytes as they possess good chemical stability, high operating potential, and flame-retardant.

1.2 Categories of SSEs

SSEs are generally categorized into solid polymer electrolytes (SPEs), inorganic ceramic electrolytes (ICEs), and solid composite electrolytes (SCEs) (Figure 1-1). Each type has limitations that prevent them from meeting all the requirements of a desirable SSE. Such requirements include high ionic conductivity, high Li^+ transference number (t_{Li^+}), high operating potential (wide ESW), sufficient interfacial compatibility (good adhesion between electrodes and SSEs and low interfacial resistance), flexibility, high thermal stability, and high mechanical strength to suppress lithium dendrites growth.

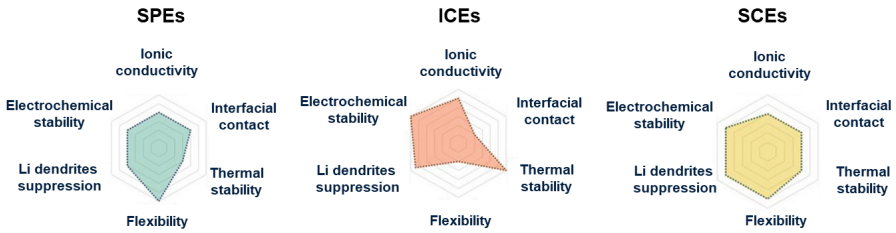

Figure 1-1. Schematic illustrations of SPEs, ICEs, and SCEs as well as their properties.[16]

SSEs typically consist of polymers (or polymer hosts), ceramic fillers, Li-salt, and additives, strongly affecting their properties. A carefully designed combination of these constituents enables SSEs to achieve the target properties demanded for LMBs. For example, polymer hosts serve as the structural framework, offering flexibility and processability while providing pathways for Li^+ migration; ceramic fillers enhance ionic conductivity, suppress polymer host crystallization, and strengthen mechanical strength, effectively preventing lithium dendrites growth. Li-salts, as the source of Li^+, significantly influence ionic conductivity, t_{Li^+}, and ESW, depending on their concentration and dissociation behavior. Additives improve ionic conductivity, optimize SSE-electrodes interfacial compatibility, and may introduce additional functionalities, such as flame retardance or self-healing properties. The following sections further explore each constituent of SSEs.

1.3 Constituents in SSEs

1.3.1 Li-salts in SSEs

For the Li-salts in SSEs, the ion–dipole interaction between the Li-salt and polymer-host impacts the Li^+ migration and influences the electrochemical stability of electrolytes.[10] Furthermore, the Li-salt participates in constructing solid electrolyte interphase (SEI) via chemical and electrochemical reactions.[11] $LiPF_6$, $LiNO_3$, lithium carboxylate, lithium sulfonate, and sulfonimides are the currently used Li-salts. Among them, the perfluorinated sulfonimide anions with a general molecular formula of $[(RF^1SO_2)(RF^2SO_2)N]^-$) have been widely studied, as they possess low affinity toward Li^+ and high structural flexibility, being beneficial to induce more free Li^+. Bis(trifluoromethanesulfonyl)imide ($[(CF_3SO_2)_2N]^-$ ($TFSI^-$) was the first perfluorinated sulfonimide anion prepared in 1972.[12] It features a -CF_3 groups with strong electron-withdrawing properties, which reduces the Lewis basicity of the anion (Gutmann donor number = 5.4[13]) and its Li^+ dissociation energy. Additionally, the -CF_3 groups may facilitate the formation of a LiF-rich SEI, which helps stabilize the cycle life of LMBs.

Identifying an economical, high-performance option from numerously available Li-salts for SSEs is critical. A lot of work has been carried out to regulate Li-salts in developing SSEs. It has been observed that both the type and chemical structure of Li-salts have a critical impact on the properties of SSEs and the formation of a LiF-rich SEI. However, it is still unclear which specific F-related factor, such as the F content or the F-connecting bonds in Li-salts, has the most significant impact on the SEI characteristics and properties of SSEs.

1.3.2 Ceramic fillers in SSEs

The ceramic fillers in SSEs can be organic, such as metal-organic frameworks (MOFs)/zeolite materials[14], or inorganic. Inorganic fillers, which are more common, can be further classified into inert and active fillers based on their ability to migrate Li^+. The inert inorganic fillers include ceramic oxides, such as Al_2O_3, TiO_2, SiO_2, novel graphene-analogue boron nitride (g-BN), etc., the ferroelectric of $BaTiO_3$,[15] and the clays.[16] Among them, ceramic oxides have gained widespread attention because of their easy synthesis, controllable size, and physical/chemical stability.

The inert inorganic fillers do not change the Li^+-conducting mechanism of polymer hosts because they are Li^+-insulated. However, when distributed in the polymer host,

firstly, they act as crosslinking centers through physical and/or chemical interactions, hindering the recrystallization of the polymer chains and thus lowering the polymer crystallinity and the corresponding glass transition temperature (T_g). Consequently, the segmental dynamics is speeding up (Figure 1-2a). Secondly, the Lewis acid-base interactions between the chemical groups on the surface of the inert inorganic fillers and the anions of the Li-salts promote the dissociation of the Li-salts, thereby enhancing the Li^+ migration (Figures 1-2b, c).[17]

The active inorganic fillers normally involve LISICON-type, perovskite-type, garnet-type, and sulfide. Compared to inert inorganic fillers, active inorganic fillers also provide a highly efficient pathway for the Li^+ migration. This indicates that, for the prepared SSEs, the polymer hosts, the active inorganic fillers, and the interface between them may contribute to the pathway for the Li^+ migration (Figure 1-2d),[18] depending on the filler content.[19] Both inert and active inorganic fillers have advantages and characterizations, while the choice of the filler type also depends on the other constituents in SSEs, and in general, the corresponding content is critical for the properties of SSEs.

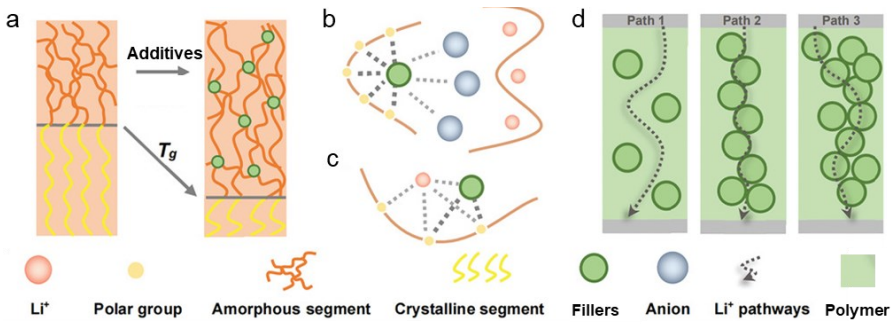

Figure 1-2. Schematic illustrations of (a) T_g change of polymer host after adding fillers, (b, c) interactions between fillers and Li-salt, and (d) Li^+ migration pathways: polymer phase (Path 1), percolated active inorganic fillers-polymer host interface (Path 2), and active inorganic fillers phase (Path 3).

1.3.3 Additives in SSEs

To reduce the crystallinity and increase the polymer host's segmental dynamics in SSEs, additives in both solid and liquid forms have been proposed. In addition, the involvement of additives can promote the Li-salt dissociation and increase the number of free Li^+ in SSEs.[20] A lot of additives have been developed, such as succinonitrile (SN), ethylene carbonate (EC), propylene carbonate (PC), dimethyl sulfoxide (DMSO),

diethyl carbonate (DEC), dimethyl carbonate (DMC), glycerol, and n, n-dimethylformamide (DMF). However, due to their flammability, volatility, corrosiveness, and poor thermal stability, they undoubtedly face a series of safety issues.[21] Additionally, their narrow ESW limits their compatibility with high-voltage cathodes. From this aspect, ionic liquids (ILs), as molten salts that remain in the liquid state and consist of positive (cation) and negative (anion) charges bound together by electrostatic interactions, have attracted considerable attention as promising alternative additives. ILs offer several advantages, including high ionic conductivity, non-flammability, a wide ESW, negligible volatility, low vapor pressure, and so on.[22] All these characteristics of ILs enable the batteries with high safe and make them operate stably within a wide ESW, in some cases, up to 6 V vs. Li/Li^+, which provides a high energy density. Currently, over a hundred ILs have been used in SSEs for various types of batteries,[23] and the number of ILs can be up to 10^{18}. Considering the designable feature of ILs, it is promising to develop SSEs using IL-additives, while selecting an appropriate IL together with the content is crucial to achieving specific requirements.

1.3.4 Polymer hosts in SSEs

Since the discovery of poly(ethylene oxide) (PEO) in 1973, numerous polymer hosts have been developed for SSEs.[24] These include polycarbonates (e.g., poly(ethylene carbonate), poly(propylene carbonate), poly(trimethylene carbonate) and poly(vinyl carbonate)), polyesters, polynitriles (e.g., polyacrylonitrile (PAN)), polyamines (e.g., polyethyleneimine), poly(vinylidene fluoride) (PVDF) and their copolymers. However, these polymer hosts show inadequate ionic conductivity and low t_{Li^+}, resulting in significant concentration-polarization at the anode during lithium plating/stripping, which compromises battery cycle life.[25] Additionally, many polymer hosts are intrinsically flammable, raising safety concerns. When liquid additives are added into polymer hosts, the prepared SSEs may experience phase separation over time due to liquid leaching, further reducing their stability.[26] Thus, the development of novel polymers with high ionic conductivity, enhanced t_{Li^+}, flame retardancy, and compatibility with liquid additives is critical for advancing SSE performance and ensuring long-term stability in LMBs.

1.4 Poly(ionic liquid)s

To further improve the performances of SSEs, a new class of polymers, poly(ionic liquid)s (polyIL), also known as polymerized ILs, have been developed. PolyILs are

formed by integrating IL molecules into one polymer chain with features of both ILs and the macromolecular architecture of polymers,[27] making them a strong alternative to conventional polymer hosts. Specifically, the advantages of polyILs are reflected in the following aspects: (i) polyILs are more electrochemically stable because they avoid the oxidation-prone C-O bond in PEO, enabling the use of high-voltage cathodes; (ii) polyILs are more compatible with their archetype IL additives, which can enhance ionic conductivity while preventing phase separation in SSEs.[28]

Even though the ionic conductivity of polyILs is higher than traditional polymer hosts, it is lower than that of the IL monomers, caused by the increase in T_g and reduction in the number of free ions from the formation of covalent bonds. Several methods can mitigate this issue: 1) substitute the anion with another one through an ion exchange reaction,[29] 2) choose an appropriate backbone or introduce a new polymer with low T_g,[30] 3) add Li-salts with low dissociation energy and weak coordination anions, such as LiTFSI,[31] 4) add small molecule organic solvents or IL additives.[32, 33] These methods have proven effective, achieving ionic conductivity up to 10^{-3} S cm^{-1} at 25 °C.[34] Figure 1-3 shows a timeline of polyIL development in the lithium batteries.

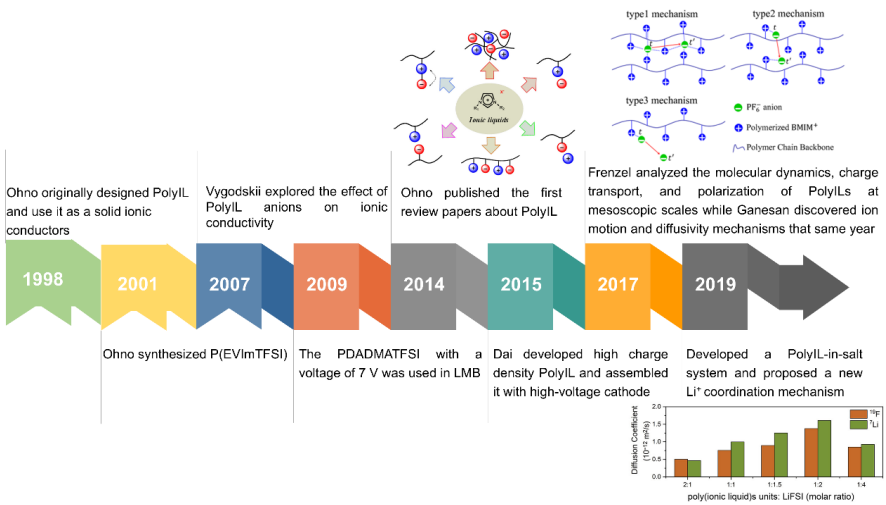

Figure 1-3. The roadmap of polyIL developed in the lithium batteries. Copy right from ref. [35, 36, 37, 38, 39, 40, 41, 42, 43].

It is worth noting that polyILs can serve not only as polymer hosts[44-47] in SSEs but also as a binder in cathodes, replacing the conventional poly(vinylidene difluoride) (PVDF) binder. PVDF is an insulating polymer that adheres to the cathode through weak van der Waals forces between C-F bonds with active materials.[48] This insulation hinders

the Li^+ diffusion within the cathodes, while the weak adhesion causes active materials to shed during extended battery cycling, ultimately shortening the battery's lifespan.[48] Instead, the polyIL binder provides strong adhesion through electrostatic interactions, helping to prolong the cycle life of batteries. PolyILs have been employed as cathode binders in LIBs, LMBs, and Li-air batteries[49], demonstrating their versatility across different battery systems. In addition, a polyIL binder was used in a thick $LiNi_{0.8}Co_{0.1}Mn_{0.1}O_2$ cathode (96 mg cm^{-2})[50] to evidence its strong adhesion.

1.5 State-of-the-art of polyIL-based SSEs

Although polyIL-based material was first designed by Ohno in 1998, their application in SSEs for LMBs was rarely reported until 2015. While great research effort has been devoted to and promising progress has been achieved, the current polyIL-based SSEs still suffer from several shortcomings: (1) low ionic conductivity[51-54] at room temperature (RT), necessitating operation at temperatures above 80 °C;[55-57] (2) limited ESWs, making them commonly paired with the LFP cathode instead of high-voltage cathodes;[33, 58, 59] (3) insufficient cycle life of the assembled cells. Additionally, (4) the commonly used doctor-blade method for preparing polyIL-based SSEs is both time-consuming and labor-intensive.

To address these limitations, further research is essential to develop polyIL-based SSEs with enhanced ionic conductivity, wider ESW, improved mechanical strength, and extended cycling life, combined with scalable fabrication for practical LMB implementation.

1.6 Research questions

PolyIL-based SSEs have demonstrated significant potential in developing LMBs, while the properties need to be further improved, and the synthesis method of SSEs needs to be effective. To develop polyIL-based SSEs with high-performance and effective synthesis-method, several research questions need to be addressed as listed below:

Q1. How do the constituents of polyIL-based SSEs influence their properties and the performance of LMBs?

Q2. How to design a polyIL-based SSE to meet the requirements of both the cathode and the lithium metal anode?

Q3. How to improve the cathode-SSE compatibility to drive the operation of high-voltage LMBs?

1.7 The aim of the thesis

This thesis aims to develop polyIL-based SSEs with enhanced properties, such as a high ionic conductivity, a wide ESW, a high t_{Li^+}, and effective suppression of lithium dendrites growth, as well as an improved compatibility with cathodes to enable LMBs operating at high cut-off voltage with extended cycle life. The specific objectives include:

(1) Identifying promising constituents for the development polyIL-based SSEs and clarifying the mechanisms driving their performance enhancements (Papers 1 and 2).

(2) Developing polyIL-based SSEs with desirable electrochemical properties (Papers 3, 4, and 5).

(3) Creating innovative methods to prepare high-performance SSEs and enhance the compatibility between the polyIL-based SSEs and cathodes (Papers 4 and 5).

1.8 Outline of the thesis

The thesis begins with reviewing of the roles of ILs in SSEs and their effects on the LMB performance (**Paper 1**), followed by investigating the impact of F-based Li-salts, specifically (lithium bis(fluorosulfonyl)imide (LiFSI), lithium bis (trifluoromethylsulfonimide) (LiTFSI), and lithium bis(pentafluoroethanesulfonyl)imide (LiPFSI)), on the properties and performance of SSEs and LMBs, as well as the mechanism of LiF formation in the SEI. (**Paper 2**). **Paper 3** examines the effect of BN nanosheet filler content on the properties of a polyIL-based SCE and the subsequent performance of LMBs. Moving on to **Paper 4**, a concentration gradient SCE was designed to simultaneously fulfill the distinct requirements of the cathode and lithium metal anode. The study examined the content of active inorganic fillers on the properties of GSCEs and compared the LMB performance utilizing GSCEs with those using uniform SCEs. **Paper 5** developed a polyIL-based SPE using a polyIL-based material host with a modified CA-polyIL substrate. The polyIL-based material also served as a cathode binder, enhancing the cathode-SPE compatibility to improve the cycle life of high-voltage LMBs.

2. Literature review on the applications of ILs in SSEs for LMBs

ILs possess high thermal stability, high solubility, low vapor pressure, high ionic conductivity, and a wide ESW, making them highly suitable for developing the SSEs of LMBs. Additionally, they can serve as precursors for synthesizing various IL-derivative materials, such as polyILs, ion gels, and IL-modified nanoparticles, highlighting their promising potential for future development.

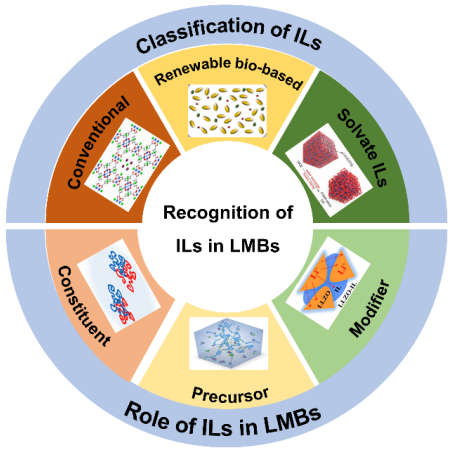

Figure 2-1. The classification of ILs and their roles in LMBs.[60-65]

In general, ILs used in SSEs for LMBs can be categorized into conventional ILs, renewable bio-based ILs (such as deep eutectic solvents, DESs), and solvate ILs (SILs), as illustrated in Figure 2-1. Conventional ILs, which can be further divided into imidazolium-, quaternary ammonium-, pyrrolidinium-, and piperidinium-based ILs, among others,[66,67] with their wide ESW, high ionic conductivity, and ability to construct effective SEI, making them suitable additives to enhance SSE properties. In contrast, DESs, which have a narrow ESW, low ionic conductivity, and weak lithium dendrite suppression capabilities, are suitable for auxiliary modifications that can reduce costs or improve targeted properties. SILs, with a narrow ESW and a coordination effect that promotes Li^+ migration, are suitable to be used as one constituent in liquid organic electrolytes or as high-conductivity auxiliary additives in SSEs.

In SSEs, ILs play several key roles due to their unique properties. First, ILs can be used as a main constituent to create ionogel electrolytes, providing high ionic conductivity and a wide ESW. Second, ILs can serve as precursors for synthesizing polyIL, which retain the wide ESW, and thermal stability of ILs while enhancing polymer-like mechanical strength. Lastly, ILs act as additives (modifiers) to enhance specific

properties of SSEs. As additives (modifiers), ILs improve ionic conductivity, broaden ESW, adjust the microstructure of SSEs, and enhance the interface stability between the SSE and electrodes, prolonging cycle life and improving the safety of LMBs. These properties make ILs highly promising in developing high-performed SSEs.

Considering the low viscosity (36±2 mPa·s), high ionic conductivity (4.70±0.03 mS cm^{-1} at 20 ℃), wide ESW (4.7 V), and low cost (750 USD/kg), 1-ethyl-3-methylimidazolium bis(trifluoromethylsulfonyl)imide (EMIMTFSI) stands out as a particularly promising additive candidate in SSEs, thus being selected for this thesis.

3. Experiments and methodology

This chapter outlines the chemicals, materials, and methods used for preparing SSEs and electrodes, as well as for assembling cells. It also covers the techniques for materials characterization and electrochemical measurements.

3.1 Chemicals and materials

Poly(ethylene oxide) (PEO, M_w~6×10^6, powder), $LiFePO_4$ (LFP), $LiCoO_2$ (LCO), $LiNi_{0.5}Co_{0.2}Mn_{0.3}O_2$ (NCM523), $LiNi_{0.8}Co_{0.1}Mn_{0.1}O_2$ (NCM811), $LiMn_xFe_{1-x}PO_4$ (LMFP), super P, polyvinylidene fluoride (PVDF, average M_w~534000.0, powder), Al foil (20.0 μm), and $Li_{6.4}La_3Zr_{1.4}Ta_{0.6}O_{12}$ (LLZTO, 300.0 nm) were obtained from MTI Corporation. Lithium bis(fluorosulfonyl)imide (LiFSI, battery grade) was purchased from DoDoChem, China. Lithium bis(pentafluoroethanesulfonyl)imide (LiPFSI, battery grade) was purchased from TCI. Lithium bis (trifluoromethylsulfonimide) (LiTFSI, battery grade) was from Jiangsu Guotai Super Power New Materials Co., Ltd, China. EMIMTFSI (99.0%) and 1-vinyl-3-butylimidazolium bis(trifluoromethyl-sulfonyl)imide (VBIMTFSI, 99.0%) were received from Qingdao Aolike New Material Technology Co., Ltd, China. Cellulose acetate (CA, DS=1.89) was supplied by Sichuan Push Acetati Co., Ltd. 2-chloropropionyl chloride (95.0%). N-butylimidazole (99.0%) was purchased from Braunway Technology. Deuterated dimethyl sulfoxide (DMSO-d6, 99.8%) was obtained from Beijing InnoChem Science & Technology Co., Ltd. 1-vinylimidazole (VIm, analytical grade (AR),), 2,2'-azobis(2-methylpropionitrile) (AIBN, AR, recrystallization), (2-bromoethyl)trimethylammonium bromide (BETAB, AR), boron oxide (B_2O_3, 98.0%, AR), 1-hydroxycyclohexyl phenyl ketone (HMPP, 99.0%), and urea (CON_2H_4, AR, 99.0%) were bought from Aladdin. Pentaerythritol tetraacrylate (PET4A), trimethylolaminomethane (Tri, >98.0%), dopamine hydrochloride (≥98.0%, powder), lithium hydroxide (LiOH, ≥98.0%, powder), ethanol (AR), acetone (>99.0%), acetonitrile (ACN, AR, >99.0%), n,n-dimethylformamide (DMF, AR, 99.5%), and 1-methyl-2-pyrrolidinone (NMP, AR, >99.0%) were purchased from Sigma-Aldrich. The above materials were used as received. The Li metal anode with a diameter of 15.8 mm and thickness of 0.1 mm was bought from China Energy Lithium Co., Ltd.

3.2 Preparation of constituents in SSEs

3.2.1 Preparation of electrospinning polyimide (PI) film

The PI powder was provided by Prof. Shuangjiang Luo, and it was synthesized using the method described in his previous work.[68] Then, 2 g PI powder was dispersed in 10 g DMF, stirring the mixture for 12 h at 60 ℃ to form a transparent solution. The Al foil was used in the negative roll of the spinning machine to collect the spinning PI fiber. The negative and positive potentials were set to -1 and 12 V, respectively, and the humidity was about 40%. The distance between the needle and the foil was 20 cm, and the spinning speed was 0.1 cm min^{-1}. Finally, the PI film was hot-pressed 3 times (110 ℃) by a roller press and dried under vacuum for 12 h at 80 ℃.

3.2.2 Preparation of polyILs

1) Synthesis of PVIm homopolymer

The synthesis scheme was adopted from the previous work,[26] which was described as follows briefly. VIm in toluene, with 1% AIBN as the initiator, was put into a three-port flask for radical polymerization. The reaction mixture was stirred under Ar at 70 ℃ for 12 h. Then, the product was washed with acetone five times. Afterward, the product was centrifugated, followed by drying in a vacuum oven at 75 ℃ for 24 h.

2) Synthesis of bromide intermediate (poly[VIm][TMEN][Br])

Poly[VIm][TMEN][Br] was synthesized by backflowing a mixture of PVIm and BETAB in a 500 g ethanol solution for 7 days at 75 ℃. Then, the bromide intermediate was washed with ethanol at 75 ℃ during the backflow to remove the unreacted BETAB. Finally, the as-obtained poly[VIm][TMEN][Br] was dried in a vacuum oven at 80 ℃ for 24 h.

3) Synthesis of poly[VIm][TMEN][TFSI]

Poly[VIm][TMEN][Br] and excess LiTFSI were dissolved in deionized water, respectively. The LiTFSI solution was added into the poly[VIm][TMEN][Br] solution, and the mixtures were stirred for 3 h at RT. After centrifugation, the white powder was washed with deionized water several times until the residual LiBr could not be detected by $AgNO_3$ (0.1 mol L^{-1}). Then, the solid powder was dried under vacuum at 90 ℃ for 24 h to obtain poly[VIm][TMEN][TFSI].

3.2.3 Preparation of BN nanosheets

The synthesis scheme was taken from the previous work[69] and described as follows.

1.64 g B_2O_3 and 24 g urea were dissolved in a mixture of 60 mL ethanol and 30 mL ultrapure water. The solution was stirred by a homogenizer and heated at 70 °C to remove the solvents for recrystallization. The white product was calcined in a tubular furnace and heated to 950 °C at a heating rate of 4 °C min^{-1} under N_2 atmosphere. As the gas was generated during the reaction, a gas exhaust system was installed at the furnace outlet. After reaching 950 °C, the tube furnace was kept for another 2.5 h. Then, the tube furnace cooled naturally to RT, and finally, the BN nanosheets with pores were obtained.

3.2.4 Modified LLZTO

200 mg Tris and 300 mg dopamine hydrochloride were dissolved into 50 mL methanol. A certain amount of LiOH was added and stirred continuously to stabilize the pH value of the solution at 8.5. Then, 3 g pure LLZTO powder was added into the solution under constant stirring. After 12 h dopamine polymerization, the color of the solution turned brown. Then, the polydopamine (PDA)-coated LLZTO particles were washed three times with methanol and dried overnight under a vacuum. Since the PDA-coated LLZTO particles were the sole fillers in Paper 4, they were still termed as LLZTO fillers.

3.2.5 Preparation of polyIL-based material

The preparation of polyIL-based material was performed via a one-step photopolymerization. Briefly, LiTFSI was dissolved in EMIMTFSI, which was denoted as Li-IL. The mixture of (VBIMTFSI, PET4A, HMPP, and Li-IL), which was termed as the polyIL-based SPE precursor solution, was put in a glass bottle and stirred for 0.5 h in a glove box at RT. Then, the mixed solution was poured into a polytetrafluoroethylene (PTFE) mold with a diameter of 16.5 cm and depth of 0.1 mm, resting for 1 h to remove bubbles. The PTFE mold was then put on a heating plate at 40 ℃, and after 0.5 h, a UV light with a wavenumber of 365 nm was employed to initiate photopolymerization. The constitute ratio was optimized step by step, i) preliminary optimizing the mass ratio between two-monomers (VBIMTFSI-PET4A); ii) optimizing the mass ratio between VBIMTFSI+PET4A and Li-IL solution under two LiTFSI concentrations (1.0 and 1.5 mol L^{-1}); iii) re-optimizing the mass ratio between VBIMTFSI and PET4A in a given Li-IL solution concentration (1.5 mol L^{-1}). The optimal ratios of constitute, along with the polymerization time, were chosen based on the results of ESW and ionic conductivity.

3.2.6 Preparation of CA-polyIL substrate

The method for preparing CA-polyIL followed the work by Zhang[70] without any modifications. Specifically, the CA-polyIL powders were dissolved in an NMP solution and stirred at RT for 24 h to form a uniform mixture. The solution was then cast onto a glass plate using a steel rod and dried in a vacuum oven at 70 °C for 24 h. The prepared samples were cut into a diameter of16 mm disks and then stored in the glove box. This step was carried out by Xinyu Ma and Yin Hu from Soochow University.

3.3 Preparation of SSEs

3.3.1 Preparation of PEO-based SPEs

The SPEs were prepared using a typical solvent casting method. Briefly, a certain amount of PEO was dissolved into ACN, and a certain amount of Li-salt (LiFSI, LiTFSI, or LiPFSI) was added. After casting, the PI film was pasted on it and dried in a vacuum oven at 50 ℃ for 24 h. Then, the prepared SPEs were cut into 16 mm disks and stored in the glove box.

3.3.2 Preparation of polyIL-based SCEs with inert fillers

To prepare the polyIL-based SCEs, the ratios of polyIL, EMIMTFSI, and LiTFSI were first fixed as (2.50:0.15:0.50) in mass after the preliminary study. Subsequently, different amounts of BN nanosheets were added, and the corresponding samples were named polyIL-0, polyIL-1, polyIL-3, polyIL-5, and polyIL-7. The detailed constituent proportion is shown in Table 3-1.

Table 3-1. The detailed constituent proportion of the polyIL-based SCEs.

Samples	polyIL (g)	EMIMTFSI (g)	LiTFSI (g)	BN (g)
polyIL-0	2.50	0.15	0.50	0.00
polyIL-1	2.50	0.15	0.50	0.01
polyIL-3	2.50	0.15	0.50	0.03
polyIL-5	2.50	0.15	0.50	0.05
polyIL-7	2.50	0.15	0.50	0.07

In the preparation, certain amounts of polyIL, LiTFSI, and EMIMTFSI with/without BN nanosheets were dissolved in NMP and mixed evenly for 10 h. Then, the mixture was poured onto the PTFE plate (diameter = 16 mm, depth = 0.3 mm) and dried in a vacuum oven at 75 ℃ for 120 h. The prepared samples were then stored in the glove box. The detailed procedure for synthesizing polyIL-based SCEs is shown in Scheme

3-1.

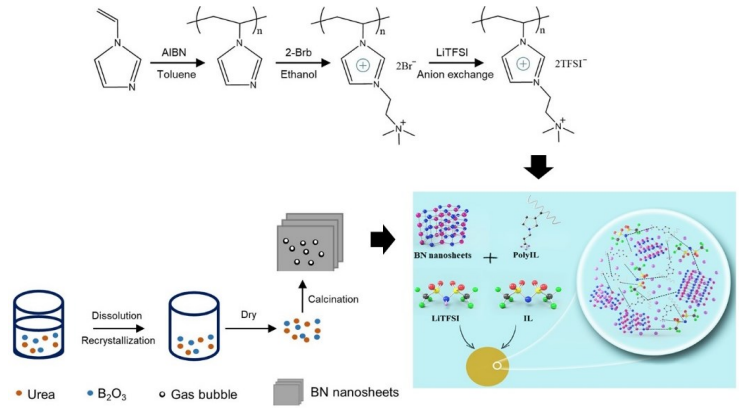

Scheme 3-1. Schematic of the synthesis process of polyIL-based SCEs.

3.3.3 One-step photopolymerization of GSCEs with multifunction

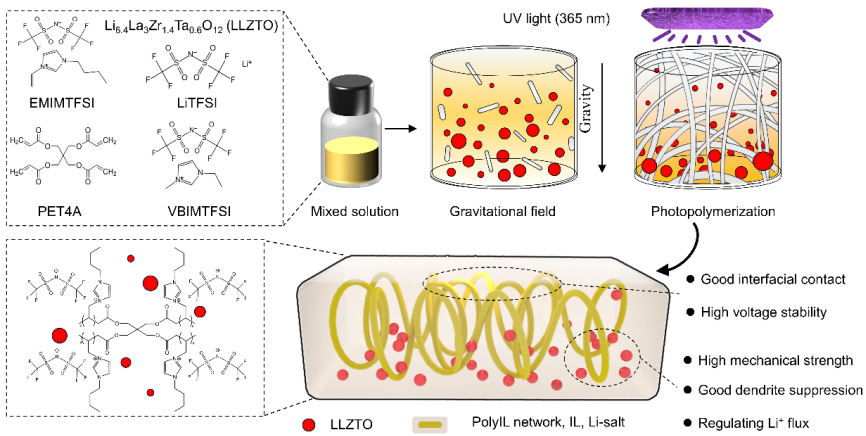

Scheme 3-2. Schematic of synthesizing GSCEs.

GSCEs were prepared via a one-step photoinitiated polymerization with HMPP as the initiator, as shown in Scheme 3-2. VBIMTFSI, EMIMTFSI, LLZTO, PET4A, and LiTFSI were thoroughly mixed in a glass bottle at RT for 5 h. Then, the mixture was poured into a PTFE mold and rested for 0.5 h. Following this, a UV light (365 nm) was employed to initiate photopolymerization, which proceeded for 16 min. After polymerization, a GSCE was obtained. The HSCE (a uniform SCE) was synthesized using the same method, but without any rest before the photopolymerization. In this study, the molar ratio of VBIMTFSI to PET4A is 8:1, the molar ratio of two monomers (VBIMTFSI+PET4A) to LiTFSI is 3:1, and the molar ratio of (VBIMTFSI+PET4A) to EMIMTFSI is 8:2. For the LLZTO fillers, three mass ratios to the two monomers were

chosen, i.e., 3, 5, and 10 wt%. The initiator was added in a weight ratio of 0.1% of the two monomers. The resulting GSCEs were designated as follows: GSCE-3 for the GSCE with 3% LLZTO fillers, GSCE-5 for 5% LLZTO fillers, and GSCE-10 for 10% LLZTO fillers.

3.3.4 Preparation of polyIL@CA-polyIL SPEs

The polyIL@CA-polyIL SPEs were prepared by immersing the CA-polyIL substrate in the polyIL-based SPE precursor solution with the optimal concentration for 10 min to achieve full penetration. Subsequently, the UV light was used to initiate the photopolymerization at 40 °C.

3.4 Preparation of cathodes

The active material (LFP/LMFP/LCO/NCM523/NCM811) and super P (80/10 wt%) were mixed and ground for 0.5 h until a uniform powder was obtained. 10 wt% optimal polyIL-based material or PVDF binder was dissolved in NMP and stirred for 12 h to form the binder solution. The binder solution was then mixed with the obtained uniform powder to form a slurry, which was vigorously stirred overnight. After that, the uniform slurry was coated onto the Al foil using a scraper and dried at 110 °C under vacuum overnight. Then, the Al foil was cut into a diameter of 14 mm disks and stored in a glove box.

3.5 Assemble coin cells

1) Ex-situ assembles coin cells

The coin cells were fabricated inside a glove box, utilizing a lithium metal anode and various cathodes (LFP/LMFP/LCO/NCM523/NCM811), with the as-prepared SSE serving as both the electrolyte and separator. During assembly, the cathode was placed at the bottom of the cell casing, followed by positioning the SSE sheet on top. The Li metal anode was then aligned and placed on the SSE sheet. A spring and spacer were added to ensure the proper contact and adjust the pressure. Finally, the positive cap was aligned, and the cell was sealed using a crimping machine. A 2025-type coin cell case was used with a sealing pressure of approximately 35 bar.

2) In-situ assembles coin cells

The coin cells were assembled in the glove box using the prepared free-standing cathode (LFP and NCM811) and CA-polyIL substrate, together with the optimal precursor solution. Briefly, a 30 μL precursor solution was dropped onto the cathode,

followed by placing the CA-polyIL substrate on the top. After 10 min, the UV light was turned on to initiate photopolymerization for 14 min. Subsequently, the Li metal anode was aligned and placed on the SSE sheet. A spring and spacer were added to ensure the proper contact and adjust the pressure. Finally, the positive cap was aligned, and the cell was sealed using a crimping machine. The coin cell case and sealing pressure used were identical to those in the ex-situ process.

3.6 Materials characterization

X-ray diffractometer (XRD) patterns were obtained from a ray diffractometer (Rigaku, Smartlab) with Cu *Kα* radiation (40 kV, 40 mA). The small angle X-ray scattering structure (SAXS) patterns were achieved on a Nano-inXider. The microstructure was examined by the scanning electron microscope (SEM, JSM-7001F), transmission electron microscopy (TEM, JEOL-2100F), and atomic force microscopy (AFM, MultiMode 8). The distribution of elements was investigated by energy dispersive X-ray (EDX) images through EDX spectroscopy. The Z-average molecular weight (M_z) and weight-average molecular weight (M_w) of polyILs and their molecular weight distribution (M_z/M_w) were determined by the gel permeation chromatography (PL-GPC50, NYSE: A).

The mechanical properties of SSEs were investigated by an electronic tensile machine (TA, Q800) with a tensile speed of 1 mm min^{-1} and atomic force microscope (AFM, Bruker, FASTSCANBIO). Thermo-gravimetric analysis (TGA, STA7200RV, Hitachi High-Tech) was conducted to analyze the thermal stability of SSEs. The coefficients of thermal expansion (CTEs) of GSCEs were tested by a thermal dilatometer (C15V). The rheological behaviors of GSCEs were characterized using a rheometer (DHR-2). The differential scanning calorimetry (DSC) analysis was performed on perkin elmer diamond DSC from -70 to 250 ℃ with a heating rate of 10 ℃ min^{-1} under the N_2 atmosphere.

For the polyIL-based SCE with BN nanosheets, the crystallinity before and after the addition of BN nanosheets was calculated according to Equation (1):

$$\chi_c = \frac{\Delta H_m}{\Delta H} \times \frac{1}{W_f} \times 100\% \qquad (1)$$

where ΔH_m is the crystallization enthalpy of the sample, which was obtained from the DSC standard data, ΔH is the enthalpy of crystallization when the sample crystallizes at 100% (i.e., -254.39 kJ mol^{-1} for BN), and W_f is the proportion of crystalline substance,

which was fitted from the detected DSC data.

Fourier transformation infrared (FT-IR) spectra was performed on a thermo nicolet 380 spectrometer over the wavenumber range of 3500-500 cm^{-1}. The chemical environments of SSEs were checked by the Raman spectrometer with an exciting laser of 532 nm (HR800 Raman spectrometer, Horiba Jobin-Yvon Ltd). The in-situ Raman was performed using a Raman spectrometer (DEEP-INRS-II). The ^{7}Li NMR spectra were acquired on a Bruker AVANCE II 400 spectrometer with NMP as the solvent. The X-ray photoelectron spectra (XPS) was performed using an ESCALAB 250Xi spectrometer. Time of flight secondary ion mass spectrometry (ToF-SIMS) was performed using PHI nanoTOFII time-of-flight SIMS under a vacuum. N_2 adsorption-desorption isotherms were recorded using a micromeritics ASAP2020.

For the peel-test, a 10-mm-wide and 30-mm-long electrode sample was attached to 3M tape, and the peel strength of the cathode specimens was measured with a high-precision micromechanical test system (Delaminator Adhesion Test System; DTS Company, Menlo Park, CA, USA). By pulling the tape at a constant displacement rate of 100 μm s^{-1}, the applied load was continuously monitored, and the force-displacement plots were made.

3.7 Electrochemical measurements

The electrochemical properties of the CR 2025-type coin cells and their performance were detected by using the CHI660E electrochemical workstation (Shanghai Chenhua Instrument Co., Ltd). The ionic conductivity (σ) of the developed SSEs was measured based on the stainless steel (SS)/SSE/SS cells by using electrochemical impedance spectroscopy (EIS) tests in the frequency ranging from 100000 to 0.1 Hz from 25 to 85 ℃ and calculated with Equation (2), where d is the thickness of the SSEs, R presents the intrinsic impedance value obtained from the EIS data, and S denotes the surface area of SS (1.95 cm^{-2} in this thesis).

$$\sigma = d/RS \qquad (2)$$

t_{Li^+} was determined by combining the measurements of alternating current impedance and direct current polarization using the Li/SSE/Li cells. Specifically, the polarization currents of the cell, including those of initial (I_0) and steady-state (I_s), were recorded under a direct current polarization potential of 50 mV (ΔV), and the interfacial resistances before (R_0) and after (R_s) polarization were tested by alternating the current impedance. Subsequently, t_{Li^+} was calculated from the Bruce-Vincent-Evans Equation

(3).

$$t_{Li+} = \frac{I_S(\Delta V - I_0 R_0)}{I_0(\Delta V - I_S R_S)} \qquad (3)$$

ESW was analyzed by the linear sweep voltammetry (LSV) in the SS/SSEs/Li cells sweeping from 1.0 to 6.0 V with a constant rate of 1 mV s^{-1}.

The Tafel plots were measured across a potential range from -0.2 to 0.2 V (vs. Li/Li^+) in the Li//Li cells using a scan rate of 1 mV s^{-1} and then managed for linear fitting.

The Li^+ diffusion energy barrier (E_d) through the SEI was determined by calculating the resistance of the Li//Li cells after 10 cycles, conducted at various temperatures (from 25 to 85 ℃), and fitting the results according to the Arrhenius law:

$$R_{SEI}^{-1} = \mathrm{Aexp}(-\mathrm{E_d}/R_g\mathrm{T}) \qquad (4)$$

where R_{SEI} corresponds to the interface impedance between the electrode and SSE, A is the conductivity pre-exponential factor, T is the absolute temperature, and R_g is the ideal gas constant (8.314 J mol^{-1} K^{-1}).

The galvanostatic intermittent titration technique (GITT) tests were performed on the CHI660E with a current density of 0.1 C and a relaxation time of 1 h per 20 min of operation during the test. The Li^+ diffusion coefficient was calculated by Equation (5).

$$D = \frac{4}{\pi\tau}\left(\frac{m_B V m}{M_B S_c}\right)^2 \left(\frac{\Delta E_s}{\Delta E \tau}\right)^2 \qquad (5)$$

where τ (s) represents the relaxation time, which was set to be 20 in this thesis; m_B (g) corresponds to the mass of the cathode active material, and M_B (g mol^{-1}) is the molar mass; S_c (cm^2) is the contact area of the electrode with the SSEs (1.53 cm^2 in this thesis), V_m (cm^3 mol^{-1}) corresponds to the molar volume of the cathode, and ΔE_s represents the change in potential due to the pulse; ΔE_τ indicates the potential difference for a constant-current plating/stripping.

The Li^+ diffusion coefficient was also calculated from the cyclic voltammetry (CV) curves by Equation (6):

$$I_P = 2.69 \times 10^5 A n^{3/2} C_0 D^{1/2} v^{1/2} \qquad (6)$$

where A, n, C_0, and v are marked as the constant, the charge transfer number (=1 in this thesis), the molar concentration of Li^+, and the scan speed, respectively.

The dendrite suppression capability and cycling performances were evaluated on a LAND battery tester (CT-2001A, Wuhan Rambo Electronics Co., Ltd.) with a potential window of 2.5-3.8 V (Li//LFP), 2.5-4.3 V (Li//LMFP), 2.8-4.3 V (Li//NCM523), 3.0-

4.5/4.8 V (Li//NCM811), and 3.0-4.3 V (Li//LCO) under different current densities.

3.8 Theoretical simulations

The theoretical simulations were conducted in cooperation with research institutions (*Institute of Process Engineering (IPE), CAS; Shenzhen HUASUAN Technology Co., Ltd*), where the results were used for analysis in this thesis. Therefore, only a brief introduction was provided in this section.

Density functional theory (DFT): the geometry of molecules was optimized through DFT. All the DFT computations were performed at the B3LYP/TZVP theoretical level with the GD3BJ dispersion correction.[71, 72]

Solvation model based on solute electron density (SMD): this model[73] was used to account for the solvation effect of MeCN. All the calculations were performed with the Gaussian 16 software package.

COMSOL: COMSOL Multiphysics 6.0 was used to track the moving boundary of the lithium sheet surface by coupling the "tertiary current distribution, Nernst Plank" interface and "deformation geometry" to simulate the process of Li^+ deposition at the interface[74]. Besides, the Nernst-Einstein equation was used to calculate the Li^+ mobility. The electrode reaction and deposition rate were described by the Butler-Walmer equation and the Faraday's law, respectively.

The *ab*-initio molecular dynamics (AIMD) simulation: it was carried out by using the projector augmented wave method in the framework of DFT[75], as implemented in the Vienna *ab*-initio Simulation Package (VASP). The generalized gradient approximation (GGA) and Perdew–Burke–Ernzerhof (PBE) exchange functional[75] were used. The Monkhorst–Pack method[76] was employed for the Brillouin zone sampling. The convergence criteria of energy and force calculations were set to be 10^{-5} eV/atom and 0.01 eV/Å, respectively. The AIMD simulations were performed by the supercells with a Gamma-centered 1 × 1 × 1 k-point grid. A small plane-wave energy cut-off of 300 eV was chosen. The time step was set to 2 fs, and all supercell systems were simulated for 10 000 steps with a total time of 20 ps in a statistical ensemble with a fixed particle number, volume, and temperature (NVT).

LAMMPS molecular dynamics simulation package with the NVT ensemble: the force field used for simulations was the universal force field.[77] The molecules, including VBIMTFSI, PET4A, EMIMTFSI, and LiTFSI were firstly optimized by ORCA in the approach of B97-3c.[72] The systems were composed of 72 VBIMTFSI, 9 PET4A, 8

EMIMTFSI, 27 LiTFSI, and 4 or 8 LLZTO clusters in low and high contents of LLZTO, respectively. The temperature was set to 300 K and maintained using a Nosé-Hoover thermostat.[78] The time step for simulations was 1 fs. The cut-off distance for the non-bonded interactions was set to 12 Å, and long-range electrostatic interactions were handled by the particle-particle particle-mesh solver. The initial configuration was generated by placing the molecules randomly in a cubic box with a side length of 40 Å. The system was first equilibrated with an NPT ensemble for 1 ns to obtain a reasonable box size. The production run was carried out for 10 ns, during which all the properties of interest were sampled and analyzed.

4. Results and discussion

In this thesis, four SSEs were developed for different purposes, and the results were summarized based on the type of SSEs.

4.1 PEO-based SPEs

The PEO-based SPEs were developed in this part in order to investigate how the configuration of F (e.g., F-contents and bond types) influences the SEI characteristics and the LiF formation mechanism, where LiFSI, LiTFSI, and LiPFSI were explicitly chosen.

To prevent cell failure resulting from the low mechanical strength of the SPE, this study employed a PI substrate. Consequently, the SPEs containing PEO and Li-salt (LiFSI, LiTFSI, or LiPFSI) on the PI substrate were denoted as PPF, PPT, and PPP, respectively. For comparison, the SPE containing only PEO on the PI substrate without Li-salt was marked as PPI.

4.1.1 Li-salts chemical structures

The chemical structures of LiFSI, LiTFSI, and LiPFSI are shown in Figure 4-1. Obviously, for LiTFSI and LiPFSI, the two sulfur (S) atoms are connected with the strong electron-attracting groups of $-CF_3$/$-CF_2CF_3$ (i.e., S-C-F), being different from the F in LiFSI (i.e., S-F). The structure with the $-CF_3$/$-CF_2CF_3$ connection can disperse negative charges, allowing the Li-salts to be dissociated easily.[79] Furthermore, the F contents in each molecule are various, which are 2F for LiFSI, 6F for LiTFSI, and 10F for LiPFSI.

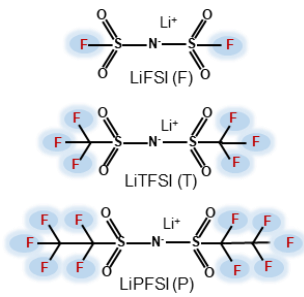

Figure 4-1. The chemical structures for LiFSI, LiTFSI, and LiPFSI.

4.1.2 Electrochemical properties and performances

The LSV curves were tested to clarify the oxidative stability of SPEs, as presented in Figure 4-2a. PPF shows a low oxidation potential, as there is a rapid increase in current at about 3.8 V, while for PPT and PPP, their oxidation occurs at a potential higher than

3.8 V. Therefore, the oxidative potentials follow the order of PPP>PPT>PPF as $V_{PPP}>V_{PPT}>V_{PPF}$. The ionic conductivities for PPF, PPT, and PPP are 0.08, 0.22, and 0.27 mS cm^{-1} at 60 °C, respectively, and their temperature-dependence is shown in Figure 4-2b. Figures 4-2c-f illustrate the impedance when using PPP, PPT, and PPF as SPEs, resulting in the t_{Li}^+ values of 0.53, 0.50, and 0.49, respectively. Combining the results here and the features of the studied Li-salts, the connecting bond of S-C-F in the studied Li-salts possesses higher ionic conductivity, t_{Li}^+, and wider ESW than those of S-F.

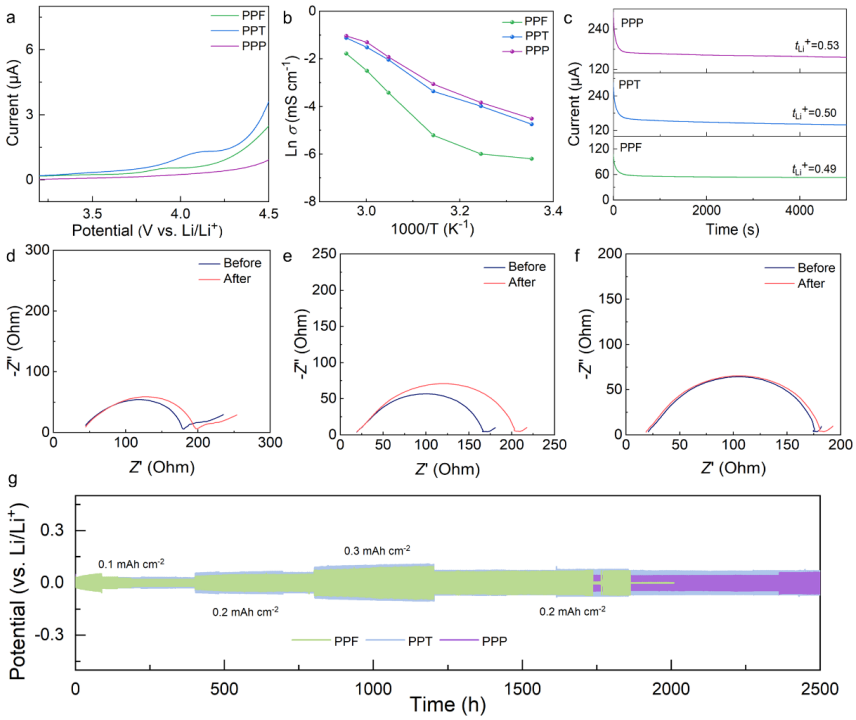

Figure 4-2. Electrochemical performances. (a) LSV curves. (b) Temperature-dependent ionic conductivity. (c) t_{Li}^+ and the Nengquist plots for (d) PPF, (e) PPT, and (f) PPP before and after polarization. (g) The Li^+ plating/stripping cycling test for Li//Li cells.

To clarify the effect of anion configuration in the Li-salts on the electrochemical performance of the Li//Li cells, their plating/stripping cycling test was carried out from 0.1 to 0.3 mAh cm^{-2} (Figure 4-2g). The overpotential of the cell using PPF drops sharply at 1900 h, evidencing a short circuit due to the lithium dendrite growth. In contrast, the cells using PPP and PPT exhibit stable cycling until 2500 h. These results show that PPP and PPT promote a robust SEI formation (increased LiF content),

suppressing lithium dendrite growth.

To further study the effects of anion configuration in the Li-salts on the cell cycling life, LMBs were assembled and tested with three representative cathodes ranging from low (LFP) to high potential (NCM523 and LCO) at 60 °C. As shown in Figure 4-3, regardless of the cathode used, LMBs incorporating PPP demonstrated slightly better or comparable cycling performance to PPT, both of which significantly outperformed PPF. Based on the observations in this work and the characteristics of the three Li-salts, it can be concluded that the anion configuration, particularly the nature of the connecting bond (S-F or S-C-F), plays a crucial role in determining the electrochemical properties and overall performance of the cells.

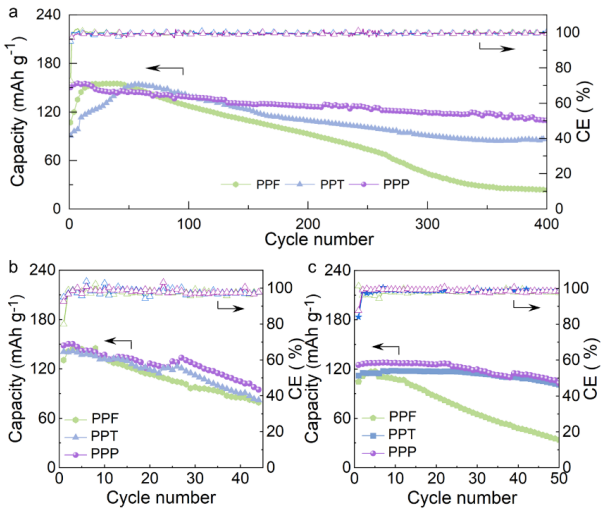

Figure 4-3. Cycling performance of LMBs using (a) LFP, (b) LCO, and (c) NCM523 cathodes at a current density of 0.5 C, 0.1 C, and 0.1 C, respectively.

4.1.3 Mechanism study

As the cell cycling life is closely related to the SEI, the XPS analysis was conducted to compare the SEI compositions in the Li//Li cells after cycling and to analyze the effect of Li-salts. The positions of elements in the XPS spectrum typically correspond to specific chemical bonds, allowing to infer the presence of specific inorganic or organic products. For clarity within the thesis, the XPS findings are visually summarized in Figure 4-4a. The detailed observations from these results are described in the following text.

(1) PPP and PPT yield an SEI containing inorganic products like LiF, Li_2O, Li_2CO_3, Li_2S, and Li_3N. However, PPF lacks Li_3N in its SEI, attributed to a salt decomposition

mechanism with predominantly 4-electron reactions generating LiF and Li_2O, while pathways involving 8-16 electron transfers leading to Li_3N or Li_2S occur less frequently.[80] The absence of Li_3N in the SEI for PPF was also supported bt the work of Budi[81]. Further, besides LiF, other inorganic species, such as Li_2O, Li_2S, Li_2CO_3, and Li_3N, positively affect the SEI characteristics by suppressing the lithium dendrite and promoting Li^+ diffusion in SEI. This observation confirms the earlier hypothesis that the absence of Li_3N in PPF contributes to the inferior cycling performance of assembled cells compared to those using PPP and PPT.

(2) As depicted in Figure 4-4b, before sputtering, there are Li-salts and LiF in the SEI, but only LiF is left after sputtering for 1 min, indicating that the Li-salt only exists on the SPE side. Moreover, the calculated F content, as illustrated in Figure 4-4c, indicates that the content of the F atom in the SEI after sputtering is increased, while the increasing degree depends on the used Li-salts. Specifically, the F atom contents were increased from 12.2% to 16.2%, 14.7% to 22.1%, and 13.0% to 24.0% when using PPF, PPT, and PPP, respectively. As only LiF exists at the lithium metal side, the F atom content also reflects the LiF content. A LiF-rich SEI plays a pivotal role in suppressing the lithium dendrite growth and facilitating the reversible cycling of LMBs. Therefore, the PPP SPE demonstrated the most optimal performance within cells.

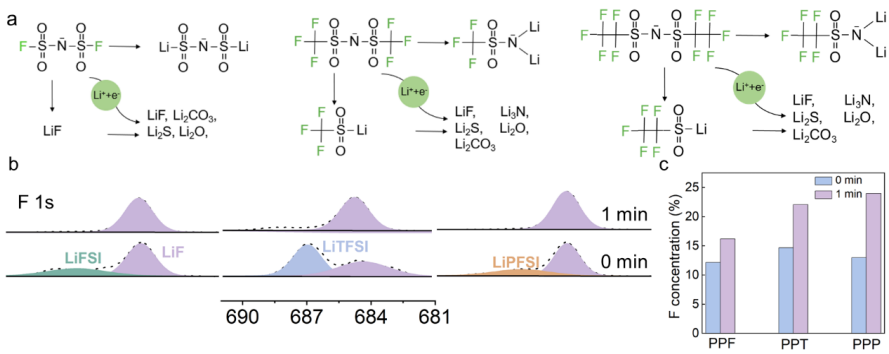

Figure 4-4. (a) The schematic illustration of the SEI composition using three Li-salts. (b) The XPS of F 1s at different etching times (from left to right: PPF, PPT, PPP) and (c) F concentration in SEI.

4.1.4 AIMD simulation of bond cleavage

Since PPP demonstrated the best electrochemical performance among the three SPEs and studies on its influence on SEI formation literature are unavailable in the existing literature, the decomposition steps for LiPFSI at different positions in the SPE to form LiF were traced through the AIMD simulations. The initial structure (Figure 4-5a)

consisted of five (5) layers of the Li atoms, the LiPFSI molecules at four (4) positions (I, II, III, IV) with different distances from the lithium metal, one (1) PI molecule, and ten (10) PEO molecules. It should be noted that the lower three layers of the Li atoms were fixed during the simulation.

For the studied LiPFSI molecules at 4 positions, the bond cleavage only occurs for Li (I) (Figure 4-5b) and Li (III) (Figure 4-5d), which are closer to the lithium metal anode (Figure 4-5a); while for Li (II) and Li (IV), no bond cleavage occurs at all (Figures 4-5c-e). Further, the orders of bond cleavages for Li (I) and Li (III) are different. For Li (I), two bonds (S2-C2 and N-S2, Figure 4-5a) are cleaved during the whole process, and the S2-C2 bond is cleaved earlier compared to N-S2. For Li (III), as depicted in Figure 4-5d, three bonds (S2-C2, N-S2, and S1-C1) are cleaved within 5 ps, and N-S2 is the first one to be cleaved among these three bonds, but there is no cleavage for the N-S1 bond. The bond cleavages reflect the LiPFSI decomposition and the formation of inorganic species, including LiF. Based on the track of the bond cleavage, the possible decomposition routes for LiPFSI to generate inorganic species were proposed as those described in reactions 1-7, where reactions 1-3 are for Li (I) position, and those of 4-7 are for Li (III) position.

The radial distribution functions of 4 LiPFSI molecules at different positions were obtained, as shown in Figures 4-5f-i. A peak arises at 2Å for Li (I)-F and Li (III)-F, while Li (II) and Li (IV) show weak signals with F but strong signals with O instead; this indicates that the LiPFSI molecule near the Li metal can generate LiF. Oppositely, the LiPFSI molecule far away from the Li metal is preferred to connect to O rather than F to generate Li_2O. It indicates that the generation of LiF is related to the position of LiPFSI to the Li metal, and only the LiPFSI molecules close to the lithium metal anode decompose and form LiF, i.e., not all the LiPFSI molecules in PPP are involved in the LiF formation. This explains why the F atom content in the inner SEI formed using PPP and PPT remains similar. Based on these findings, it can be concluded that the F-connecting bond in the Li-salt is more critical than the F atom content for generating a LiF-rich SEI.

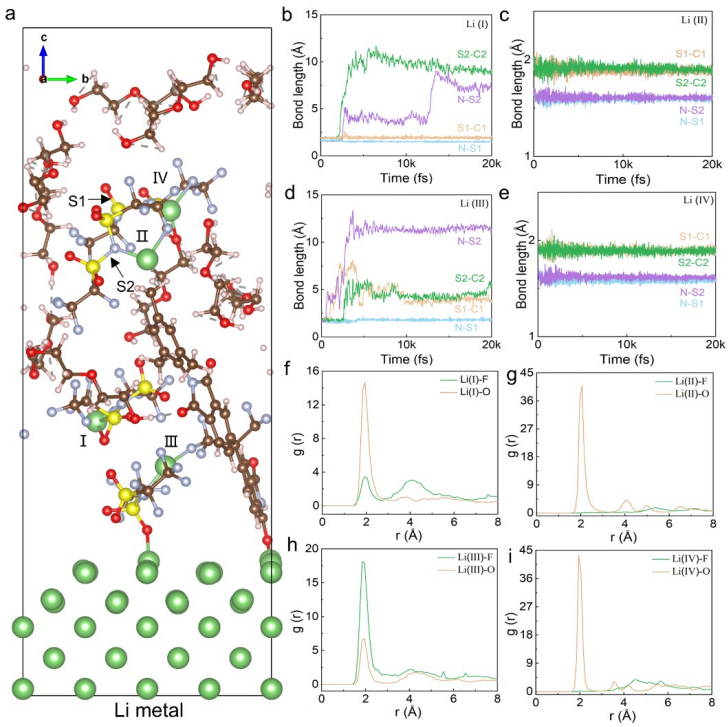

Figure 4-5. Probability distribution functions of Li^+ with F and O elements. (a) The simulation structure of SPE and Li metal anode. Bond cleavage of (b) Li (I), (c) Li (II), (d) Li (III), and (e) Li (IV). Radial distribution functions of (f) Li (I)-F/O, (g) Li (II)-F/O, (h) Li (III)-F/O, and (i) Li (IV)-F/O.

$$LiN(SO_2C_2F_5)_2 + ne^- + nLi^+ \rightarrow Li_3N + Li_2S_2O_4 + LiF + C_2F_xLi_y \quad (1)$$

$$Li_2S_2O_4 + 4e^- + 4Li^+ \rightarrow Li_2SO_3 + Li_2S + Li_2O \quad (2)$$

$$C_2F_xLi_y + ne^- + nLi^+ \rightarrow 2Li_2CO_3 + LiF \quad (3)$$

$$LiN(SO_2C_2F_5)_2 + 3e^- + 3Li^+ \rightarrow Li_2NSO_2C_2F_5 + LiSO_2C_2F_5 \quad (4)$$

$$Li_2NSO_2C_2F_5 + LiSO_2C_2F_5 + ne^- + nLi^+ \rightarrow Li_3N + Li_2S_2O_4 + C_2F_xLi_y \quad (5)$$

$$Li_2S_2O_4 + 4e^- + 4Li^+ \rightarrow Li_2SO_3 + Li_2S + Li_2O \quad (6)$$

$$C_2F_xLi_y + ne^- + nLi^+ \rightarrow 2Li_2CO_3 + LiF \quad (7)$$

4.1.5 Sub-summary

In this part, the effect of the anion configuration in the Li-salts on the formation and composition of the formed SEI in LMBs was studied. It shows that the F-connecting bond in the Li-salts is more important than the F element contents, and thus, the

performances of SPEs and cells using LiPFSI are slightly better than LiTFSI and much better than LiFSI. After comparing the prices of LiPFSI (817 USD/10-g) and LiTFSI (156 USD/10-g), LiTFSI was selected for the subsequent research.

In the present study, PEO was utilized as the polymer host with the single addition of Li-salts. This approach is economical, but the enhancement of electrochemical performance is limited, especially in the cycling life of cells. Seeking alternative polymers is important, where polyIL with wide ESW and high ionic conductivity can be a desirable candidate. Incorporating inert inorganic fillers into the polymer host can also boost the Li^+ migrate and overall ionic conductivity, and IL additive has been suggested to improve the ionic conductivity. Therefore, the further work was conducted on these aspects to improve the performance of SSEs.

4.2 PolyIL-based SCEs with inert fillers

In this part, an SCE was synthesized using a template method to investigate the effect of inert inorganic filler content on the properties of polyIL-based SCEs and the performance of LMBs. The polyIL of poly [VIm][TMEN][TFSI]) was chosen as the polymer host due to its relatively low operation temperature and high ionic conductivity. BN nanosheets, with a high specific surface area and a porous structure, were used as the inert inorganic filler to homogenize the Li^+ flux and facilitate Li^+ migration. EMIMTFSI, which has low viscosity and high ionic conductive, was incorporated to reduce the interfacial resistance.

4.2.1 Characteristics

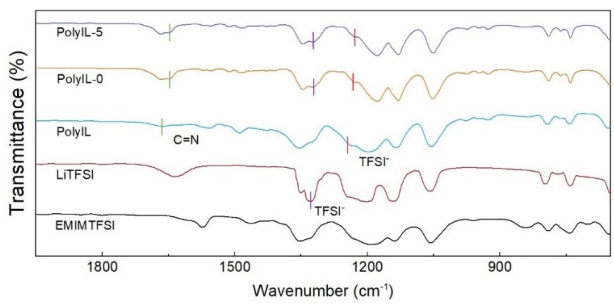

Figure 4-6. FT-IR spectra of polyIL-based SCEs and constituents.

The chemical structure of the polyIL was analyzed using FT-IR spectra (Figure 4-6). The adsorption peaks at 1643 and 1135 cm^{-1} correspond to C=N and C-N stretching vibrations of the imidazole ring, respectively. An additional adsorption peak at 1488 cm^{-1}, attributed to the C-N vibration of the tetraalkylammonium cations, and

characteristic peaks at 1326, 1241, and 1056 cm^{-1}, associated with $TFSI^-$, confirm the successful synthesis of poly [VIm][TMEN][TFSI]. Upon adding LiTFSI and EMIMTFSI (polyIL-0), the -SO_2 stretching vibration peak of LiTFSI shifts from 1171 to 1169 cm^{-1}, indicating that more carbonyl groups are involved in lithium bond formation.[82] After introducing BN fillers (polyIL-5), the FT-IR spectra remain consistent with that of polyIL-0, confirming the absence of new bond formation between polyIL-0 and the BN nanosheet fillers.

4.2.2 Electrochemical properties

PolyIL-based SCEs with varying amounts of BN nanosheets were investigated to obtain their electrochemical properties. Figure 4-7a shows the ionic conductivities at different temperatures. Initially, the ionic conductivities increase and then decrease with increasing the content of BN nanosheets. Among the cases studied, polyIL-5 exhibits the highest ionic conductivity, reaching 0.16 mS cm^{-1} at 25 ºC and 1.49 mS cm^{-1} at 85 ºC. Furthermore, their ESWs were assessed, as shown in Figure 4-7b. The results indicate that the oxidation potential of polyIL-0 to polyIL-7 increases and then decreases, attributed to the properties and dispersion of BN nanosheets within the SCEs. The current of polyIL-5 maintains a constant until 5.1 V, indicating a wide ESW. Considering both the ionic conductivity and ESW results, polyIL-5 is considered the optimized choice. Figure 4-7c shows the DC polarization curve of polyIL-5, and the estimated t_{Li^+} of polyIL-5 is 0.53. In contrast, the t_{Li^+} value of polyIL-0 is lower than that of polyIL-5 (Figure 4-7d).

The strain-stress curves were determined to evaluate the mechanical properties of SCEs. As shown in Figure 4-7e, the tensile strength of polyIL-5 is 0.45 MPa with an elongation-at-break of 180%. For comparison, the tensile strength of polyIL-0 is only 0.16 MPa with an elongation-at-break of 170%. The enhanced tensile strength can be attributed to the high Young's modulus of BN (Young's modulus of monolayer (1L) BN is as high as 0.71-0.97 TPa[83]), which is in line with the second reinforcement theory.[84, 85]

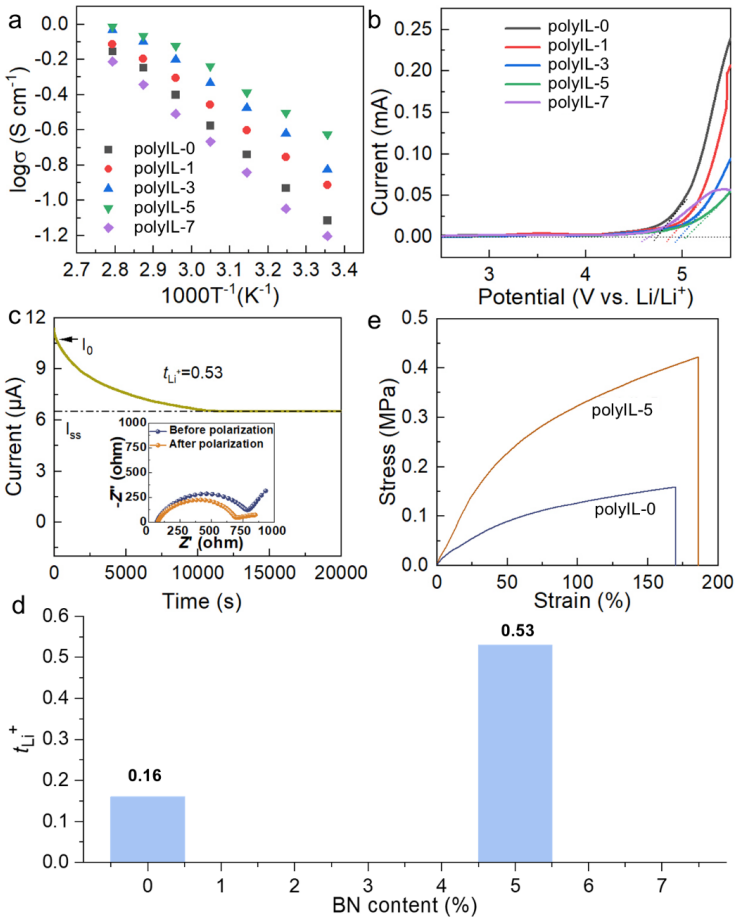

Figure 4-7. (a) Arrhenius plots, (b) LSV curves of polyIL-based SCEs with various amounts of BN nanosheets, and (c) DC polarization curve of polyIL-5, the insert image is the EIS curves before and after polarization, (d) Comparison of t_{Li}^{+}, (e) Strain-stress curves.

4.2.3 Interface stability and cell performances

To further identify the positive effect of polyIL-5 compared to polyIL-0 in suppressing the lithium dendrite growth, the cycling was recorded on the Li//Li cells at a current density of 0.5 mA cm^{-2}. As shown in Figure 4-8a, the overpotential of Li//Li cells with polyIL-5 and polyIL-0 is remarkably constant during the whole cycling of 600 h, but the one with polyIL-5 deliver a much lower overpotential, which implies that polyIL-5 can regulate Li^{+} diffusion near the anode and achieve stable lithium plating/stripping cycling. In fact, the Lewis acid-base interaction between $TFSI^{-}$ and B plays the role of "ionic selector", which generates free Li^{+} in the system, alleviating the generation of

high polarization potentials at the polyIL-0/lithium metal interface, consistent with the t_{Li^+} values in Figure 4-7d.

The Li//LFP cell with polyIL-5 exhibits a good rate capability (Figure 4-8b), delivering high discharge specific capacities of 152, 147, 143, and 141 mAh g^{-1} when cycled at 0.1, 0.3, 0.5, and 1 C, respectively. Such desirable results are attributed to the high ionic conductivity and high t_{Li^+} of polyIL-5. Figure 4-8c shows the corresponding cycling performance and Coulomb efficiency of the Li/polyIL-5/LFP cell at a current density of 0.1 C at 55 ºC. It can be seen that a maximum discharge specific capacity of 154 mAh g^{-1} is maintained after 300 cycles, and the Coulombic efficiency is greater than 99.0%.

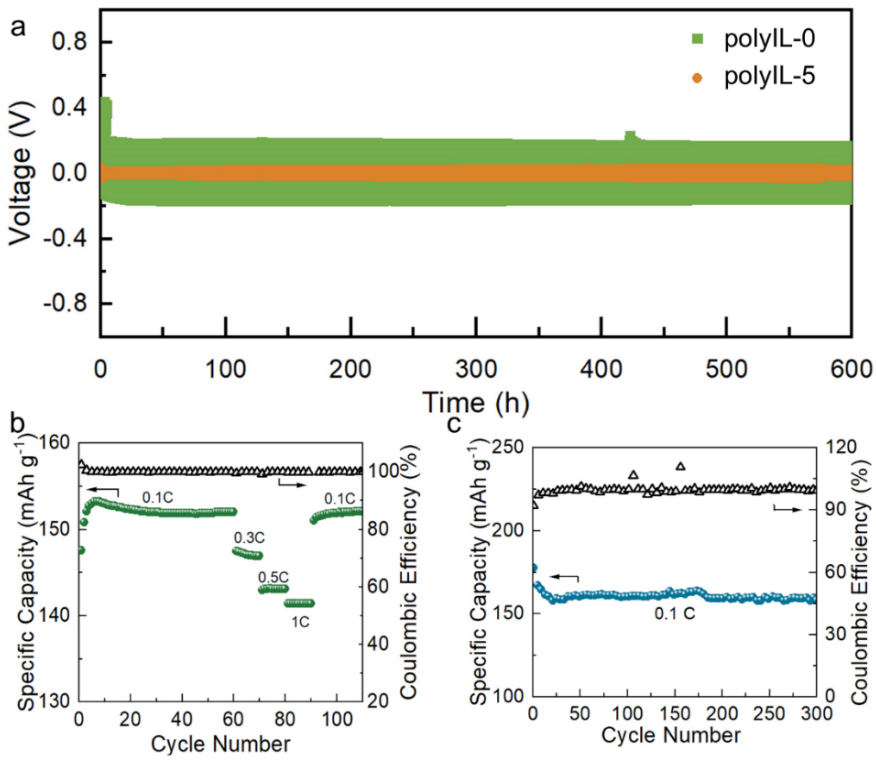

Figure 4-8. (a) Cycling for polyIL-5 and polyIL-0 in Li//Li cells. (b) The rate and (c) cycling performance of Li//LFP cells with polyIL-5.

4.2.4 Sub-summary

This part demonstrats that the properties of polyIL-based SCE, including ionic conductivity, ESW, and t_{Li^+} are related to the content of BN nanosheets. These properties initially increase and then decrease as the BN nanosheet content rises, with

a percolation threshold of 1.6 wt% (polyIL-5). The Li/polyIL-5/LFP cell retains a maximum discharge specific capacity of 154 mAh g^{-1} after 300 cycles.

While the polyIL-based SCEs exhibit better electrochemical performance than the PEO-based SPE, their compatibility with high-voltage cathodes remains unclear. Furthermore, polyIL-based SCEs face challenges in meeting the different requirements of both electrodes, where the cathode-side needs essential flexibility and high-voltage stability, while the anode-side should possess good interfacial contact and enough strength to suppress the lithium dendrites growth. Moreover, the non-conductive nature of BN inert inorganic fillers, combined with the high binding energy between inorganic particles, poses a risk of uneven dispersion, potentially hindering the Li^+ migration.

4.3 GSCE with multifunction

Multilayer SCEs offer the potential to meet the distinct requirements of both cathodes and lithium metal anodes, but their development is hindered by high interlayer resistance and complex preparation methods. To overcome these challenges while retaining their benefits, a natural sedimentation strategy was developed to create concentration gradient SCEs (GSCEs) with multifunction. The polyIL-rich side contacting with the cathode provides superior flexibility and enhanced antioxidation capability, while the $Li_{6.4}La_3Zr_{1.4}Ta_{0.6}O_{12}$ (LLZTO)-rich side, which is tailored for the lithium metal anode, ensures excellent interfacial contact and mitigates lithium dendrite growth. To further improve performance, the LLZTO particles were modified with PDA, enabling uniform dispersion within the GSCE.

4.3.1 Characteristics

FT-IR spectra was conducted to investigate the molecular structure of polyIL and GSCEs, as shown in Figure 4-9. The C=C stretching band of VBIMTFSI and PET4A monomers, located around 1658 cm^{-1}, almost disappeared after polymerization. Concurrently, the absorption bands at around 1469 and 916 cm^{-1}, which are ascribed to the end C=C-H shearing and out-of-plane bending vibration of the VBIMTFSI monomer, respectively, also vanished after polymerization.[86, 87] These results indicate the successful synthesis of polyIL from VBIMTFSI and PET4A. Comparing the FT-IR spectra of polyIL and GSCE-0 (polyIL with EMIMTFSI and LiTFSI, no LLZTO included) evidences that there are no discernible changes, implying that EMIMTFSI and LiTFSI do not alter the molecular structure of polyIL. However, upon incorporating LLZTO nanoparticles, e.g., from GSCE-3 to GSCE-10, the vibrational peak in polyIL

at 1180 cm^{-1}, which is assigned to -CF_3 of $TFSI^-$, experiences continuous red-shifts, suggesting a reshaped coordination environment derived from the interaction between polyIL with EMIMTFSI and LiTFSI in GSCEs and LLZTO.

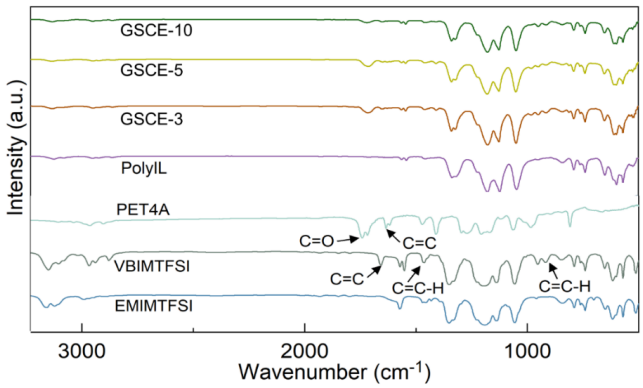

Figure 4-9. The FT-IR spectra.

To determine the optimized ratio of LLZTO content in GSCEs, the GSCEs were characterized with different techniques, including the rheological behaviors, thermal dilatometer, Raman, and ^{7}Li NMR. Combining all the characterizations, GSCE-5 was identified as the most favorable choice, attributed to its abundance of Li^+ migrate sites and its faster Li^+ migrate kinetics.

For the GSCE with the optimal LLZTO ratio (GSCE-5), a cross-sectional SEM image reveals a thickness of 400 μm (Figure 4-10a). The SEM images of the upper, middle, and lower layers within the cross-section were further analyzed, as shown in Figure 4-10b. To investigate the distribution of zirconium (Zr) elements in each layer, EDS mapping was performed, with the results presented in Figure 4-10c. The upper layer (#1), corresponding to the LLZTO-rich side, exhibits the highest Zr concentration (9.26%), while the lower layer (#3), representing the polyIL-rich side, shows a Zr concentration of 4.97%. The middle layer (#2) displays an intermediate Zr concentration of 5.81%. These results highlight a gradual decrease in Zr concentration from the upper to the lower layers, confirming the formation of a gradient distribution of LLZTO nanoparticles within GSCE-5.

The mechanical strength and interfacial stability of GSCE-5 were evaluated by measuring Young's modulus through AFM mapping. As illustrated in Figures 4-10d-e, the polyIL-rich side of GSCE-5 exhibits a lower Young's modulus of 6.4 MPa, being desirable to establish superior contact with the cathode.[88, 89] Conversely, the LLZTO-

rich side of GSCE-5 exhibits a higher Young's modulus of 13.9 MPa, which is more than twice that of the polyIL-rich side, effectively aiding in suppressing lithium dendrite growth. The distinct variations in Zr content and Young's modulus on both sides serve as evidence supporting the existence of a Zr concentration gradient structure within the GSCE-5.

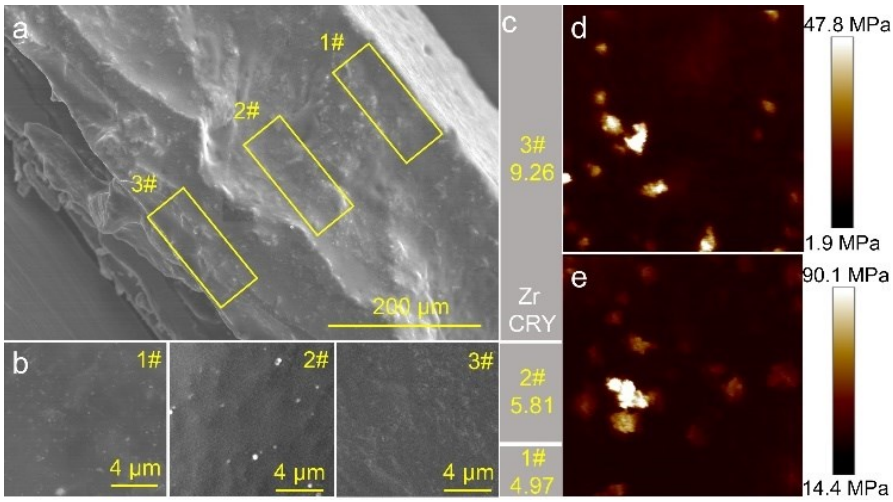

Figure 4-10. (a) Cross-sectional and the zoom (b) in SEM images of upper (1#), middle (2#), and under (3#) parts of layer highlighted by yellow of GSCE-5. (c) The ratio of Zr content in different layers. The AFM images of Young's modulus mappings of (d) polyIL-rich and (e) LLZTO-rich sides of GSCE-5.

4.3.2 Electrochemical properties and performances

To substantiate the enhanced electrochemical performances attributed to the concentration gradient structure, a series of electrochemical experiments were conducted to obtain such as ionic conductivity, t_{Li^+}, ESW, and cell cycle life. These discernments were subsequently compared with those of a uniform hybrid solid composite electrolyte (designated as HSCE-5). Figure 4-11a shows that GSCE-5 has a high ionic conductivity of 4.53×10^{-4} S cm^{-1} at 25 ℃, increasing to 9.66×10^{-4} S cm^{-1} at 65 ℃, with a t_{Li^+} value estimated at 0.45. In comparison, the HSCE-5 displays an ionic conductivity of 1.03×10^{-4} S cm^{-1} at 25 ℃, reaching 7.36×10^{-4} S cm^{-1} at 65 ℃, with a t_{Li^+} value estimated at 0.27 (Figure 4-11b). These results imply that GSCE-5 is likely to reduce polarization and enhance the fast-charging capability of cells. The ESWs of GSCE-5 and HSCE-5 were investigated using LSV (Figure 4-11c). In the Li/GSCE-5/SS cell, the lithium metal was in contact with the LLZTO-rich side, while the SS working electrode was in contact with the polyIL-rich side. The GSCE-5 exhibits

an electrochemical anodic stability of up to 5.6 V vs. Li/Li^+, greater than that of HSCE-5 (4.9 V vs. Li/Li^+). However, both SCEs exhibit high anti-oxidation stability to match high-voltage cathodes (usually 4.3 V vs. Li/Li^+).

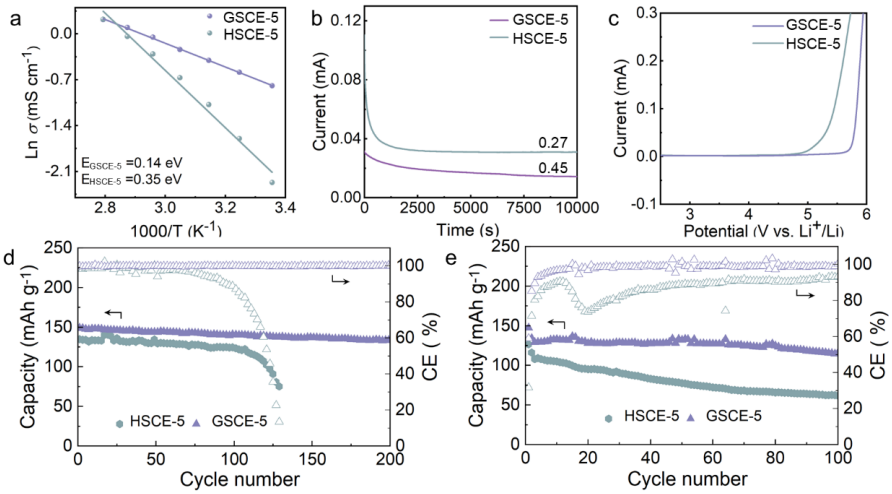

Figure 4-11. (a) Ionic conductivity, (b) current–time curves, and (c) LSV curves for GSCE-5 and HSCE-5. Cycling stability of LMBs that used (d) LFP and (e) LFMP cathodes, respectively.

Furthermore, the feasibility of utilizing GSCE-5 and HSCE-5 in practical applications was evaluated using low-voltage LFP (2.5-3.8 V) and high-voltage LMFP (2.5-4.3 V) cathodes in Li//LFP (LMFP) cells. As shown in Figure 4-11d, the initial discharge specific capacities of the Li//LFP cell with GSCE-5 and HSCE-5 at a current density of 0.2 C are 148.8 and 134.7 mAh g^{-1}, respectively, demonstrating high specific capacity of using GSCE-5. Moreover, the cell using GSCE-5 exhibits excellent initial capacity retention of 89.6% after 200 cycles (133.3 mAh g^{-1}), whereas the one with HSCE-5 retains only 55.9% of its initial specific capacity (75.3 mAh g^{-1}) after 130 cycles. The Coulombic efficiency of using GSCE-5 exceeds 99.7%, surpassing that of the HSCE-5 (<99.0%). Meanwhile, in the Li/GSCE-5/LMFP cell (Figure 4-11e), an initial discharge capacity of 147.4 mAh g^{-1} is achieved at a current density of 0.2 C, which retains 115.9 mAh g^{-1} after 100 cycles with a Coulombic efficiency of higher than 94.4%. Conversely, the Li/HSCE-5/LMFP cell experiences rapid specific capacity fade, with a capacity retention of only 48.9% of its initial specific capacity.

4.3.3 Sub-summary

GSCEs were fabricated using a natural sedimentation strategy combined with a UV-

curing polymerization technique for LMBs. Experimental results confirm the formation of a LLZTO concentration gradient structure within the SCE. Among the GSCEs with varying filler contents, a 5wt% filler content was identified as optimal. Compared to uniform SCE-5, the GCSE-5 demonstrates higher ionic conductivity, a higher t_{Li^+}, and a broad ESW, leading to the Li/GCSE-5/LMFP cell operated at a cut-off potential of 4.3 V and exhibited a capacity retention of 89.6% after 100 cycles.

A natural sedimentation strategy was developed to construct concentration GSCEs with multifunction, the electrochemical properties of the GSCEs (with active inorganic fillers) were improved compared to the polyIL-based SCEs with inert inorganic fillers, and they are compatible with high-voltage cathode. However, the cycle life of the assembled LMBs remains insufficient. This limitation may stem from the non-uniform distribution of inorganic fillers within the polymer host and variations in their surface energies. Furthermore, the compatibility of the cathode-SSE interface is critical for achieving the long cycle life of LMBs. However, this aspect remains underexplored in this part.

4.4 PolyIL@CA-polyIL SPEs

SSEs offer significant potential in LMBs but are hindered by large SSE-electrode interfacial resistance and their limited interfacial compatibility. In this part, a novel polyIL-based SPE was developed by combining a polyIL-based material host (identical to the polymer in *Part 4.3*) with a modified cellulose acetate (CA)-polyIL substrate enriched with diverse functional groups. The impact of the modified CA-PoyIL substrate on the properties of the SPE was systematically evaluated and analyzed. As the polyIL-based material demonstrated strong adhesion, high ionic conductivity, and excellent antioxidant stability, it was used to serve as a cathode binder together with the in-situ photopolymerization cell assembly method for enhancing the SPE-electrode compatibility and enabling LMBs to achieve a long cycle life. For comparison, a PVDF binder-based cell was also assembled.

4.4.1 Characteristics

The chemical composition of the synthesized polymers was analyzed using FT-IR spectra. As shown in Figure 4-12, the C=C stretching band at 1658.4 cm^{-1} and the C=C-H at 1469.4 cm^{-1} of the VBIMTFSI monomer almost disappeared, and the intensity of the C=C peak of PET4A at 1637.2 cm^{-1} weakened, indicating that VBIMTFSI and PET4A monomers are successfully polymerized into polyIL. Furthermore, after adding

the Li-IL solution, all C=C peaks associated with VBIMTFSI and PET4A vanished, suggesting that the Li-IL solution facilitated the polymerization reaction. The C=N peak at 1747.5 cm^{-1}, belonging to CA-polyIL, weakened after the polymerization with the polyIL-based SPE precursor solution, indicating that polyIL-based SPE is cross-linked with the $TFSI^-$ of CA-polyIL. In addition, the C=O region in polyIL@CA-polyIL SPE shifted compared to that in polyIL-based SPE (e.g. 1743.7 vs 1667.1 cm^{-1}), suggesting the formation of a cross-linking complex through the interaction of Li^+ with the C=O, which provides an additional Li^+ migrate pathway.[90]

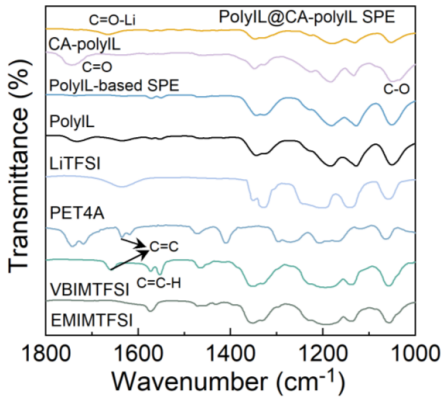

Figure 4-12. The FT-IR spectra.

4.4.2 Electrochemical properties and performances

Various electrochemical measurements were performed to demonstrate the impact of CA-polyIL on the performances of SPEs. The polyIL@CA-polyIL SPE presents the superior ionic conductivity of 0.12 mS cm^{-1} at RT and 1.20 mS cm^{-1} at 85 °C, compared with 0.05 and 0.76 mS cm^{-1} of polyIL-based SPEs, respectively (Figure 4-13a). The t_{Li^+} of the polyIL-based SPE is 0.15 (Figure 4-13b), which is lower than the polyIL@CA-polyIL SPE of 0.28 (Figure 4-13c). This improvement is attributed to the negatively charged -OH and C=O groups in the modified CA, which effectively coordinate with Li^+ and provide additional pathways for Li^+ migration.

The intrinsic oxidative stability of SPEs was tested using LSV. As shown in Figure 4-13d, the oxidative decomposition potential of polyIL-based SPE is around 5.2 V, whereas CA-polyIL exhibits a maximum antioxidation potential of approximately 4.8 V, due to the presence of terminal -OH.[91] However, due to the low proportion of CA-polyIL in the polyIL@CA-polyIL SPE, the antioxidation potential of polyIL@CA-polyIL SPE remains the same as that of polyIL-based SPE at 5.2 V.

To further characterize the practical oxidation stability of SPEs in LMBs, an electrochemical floating test was carried out in Li//NCM811 cells, where the measured leakage current serves as a direct indicator of oxidation stability (Figure 4-13e). The leakage current remains very low at a high potential of 5.0 V (<0.04 mA) for both polyIL-based SPE and polyIL@CA-polyIL SPE, demonstrating their superior compatibility with high-voltage cathodes.[92]

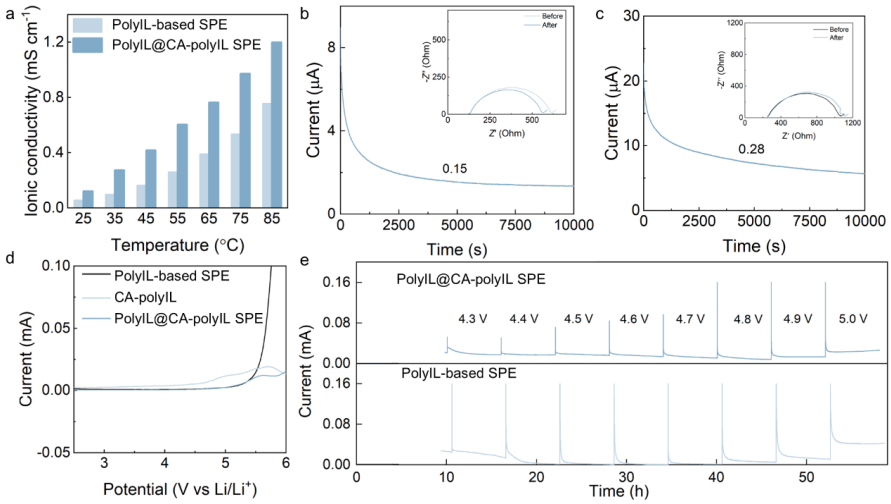

Figure 4-13. (a) Ionic conductivity. Chronoamperometry and EIS curves of (b) polyIL-based SPE and (c) polyIL@CA-polyIL SPE. (d) LSV curves. (e) Electrochemical floating test for Li//NCM811 cells.

The interfacial stability during the Li^+ plating and stripping process was investigated to determine the critical current density (CCD) of SPEs. As shown in Figures 4-14a-b, the CCDs of polyIL-based SPE and polyIL@CA-polyIL SPE are 0.2 and 1.5 mA cm^{-2}, respectively, due to the high t_{Li^+} of polyIL@CA-polyIL SPE. Subsequently, the prolonged Li^+ plating and stripping process of SPEs at 0.1 mA cm^{-2} was compared (Figures 4-14c-d). While the polarization potential of polyIL-SPE is stabilized, it eventually fails after 1369 h. In contrast, the polyIL@CA-polyIL SPE maintains a stable Li^+ plating and stripping process for over 3300 h.

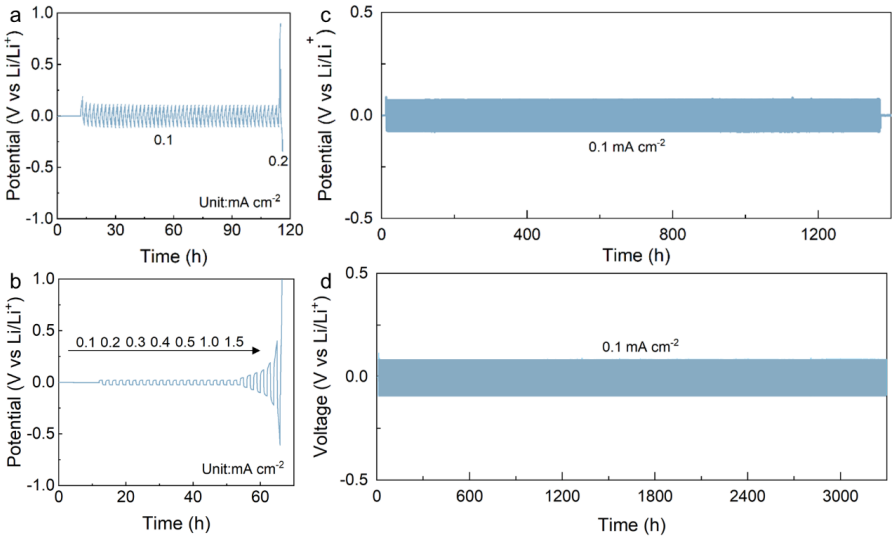

Figure 4-14. Potential curves of Li//Li cells with (a and c) polyIL-based SPE and (b and d) polyIL@CA-polyIL SPE.

4.4.3 Properties of binders and their Li^+ diffusion capacity within LFP cathode

The adhesion strength between the binder and the current collector is a key factor in assessing the cathode's durability. As demonstrated by the peeling test shown in Figure 4-15a, the LFP with the polyIL-based binder maintains a steady peeling force of 0.6 N for approximately 700 s, demonstrating superior flexibility and sustained adhesion. In contrast, the LFP cathode with a PVDF binder initially shows a higher peeling force of 1.2 N, which decreased to 0.7 N after 300 s and then failed rapidly around 350 s. Further, the interfacial wettability between the precursor solution and the LFP cathode was assessed via contact angle measurements (Figure 4-15b). The results reveal that the LFP cathode with the polyIL-based binder exhibits superior wettability than that with the the PVDF binder. This enhanced wettability, resulting from the shared constituents between the polyIL-based binder and the precursor solution of polyIL-based SPE, improved the overall cathode-polyIL@CA-polyIL compatibility.

The D_{Li}^+, a key parameter for characterizing electrode kinetics, was calculated from the CV and GITT measurements. The results are presented in Figure 4-15c. Although the D_{Li}^+ values calculated by the two methods are not completely consistent, both indicate that the Li^+ diffusion rate in the LFP with the polyIL-based binder is higher than that with the PVDF binder. The outstanding Li^+ diffusion rate results from the high ionic conductivity of polyIL-based binder and the established continuous conducting

networks. The enhanced Li^+ diffusion rate further contributes to cells achieving stable cycle life and Coulombic efficiency.

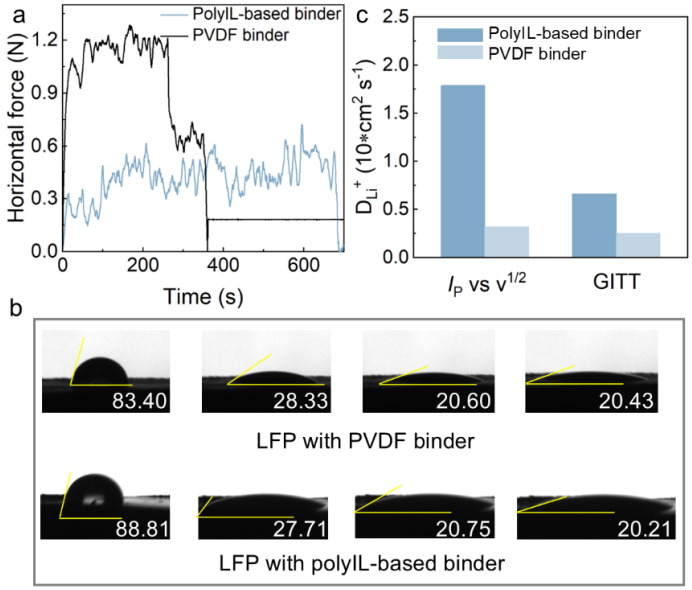

Figure 4-15. (a) Peeling tests for LFP with various binders. (b) Contact angle measurements of LFP with PVDF and polyIL-based binders. (c) Comparation of D_{Li}^+ obtained through different methods.

4.4.4 Compatibility verification

The impact of cathode-SPE compatibility on cell performance was evaluated using the low-voltage LFP and high-voltage NCM811 cathodes with different binders. The in-situ fabrication scheme of LMB is illustrated in Figure 4-16a. First, the cycle life of Li//LFP cells was evaluated, as shown in Figures 4-16b-c. The cell with the polyIL-based binder exhibits an initial discharge specific capacity of 122.9 mAh g^{-1}, retaining 84.5% initial capacity after 1100 cycles at 0.5 C. In contrast, although the cell with the PVDF binder initially delivers a higher specific capacity of 172.0 mAh g^{-1}, its specific capacity drops to 85.7 mAh g^{-1} after 830 cycles, reflecting a poor capacity retention of 49.8%. As all other components, except for the binder, of the cell remained identical, the excellent cycling stability for the Li//LFP cell with the polyIL-based binder can be attributed to the shared composition between the binder and the SPE, i.e., polyIL-based materials that enhance Li^+ diffusion within the cathode and the reduced interfacial resistance.

Furthermore, cells using an NCM811 cathode with polyIL-based binder and a Li anode

were assembled. As illustrated in Figure 4-16d, the Li//NCM811 cell operated within a potential range of 3.0-4.5 V delivers a high initial specific capacity of 145.5 mAh g^{-1} and maintains a stable cycling life for over 200 cycles, with a capacity retention of 94.9%. When the Li//NCM811 cell operates at an extended potential range of 3.0-4.8 V (Figure 4-16e), it achieves a high specific capacity of 178.1 mAh g^{-1} at 0.1 C and retains 95.4% of its initial specific capacity after 100 cycles. This high level of working potential surpasses results reported in published literature, as shown in Table 4-1.

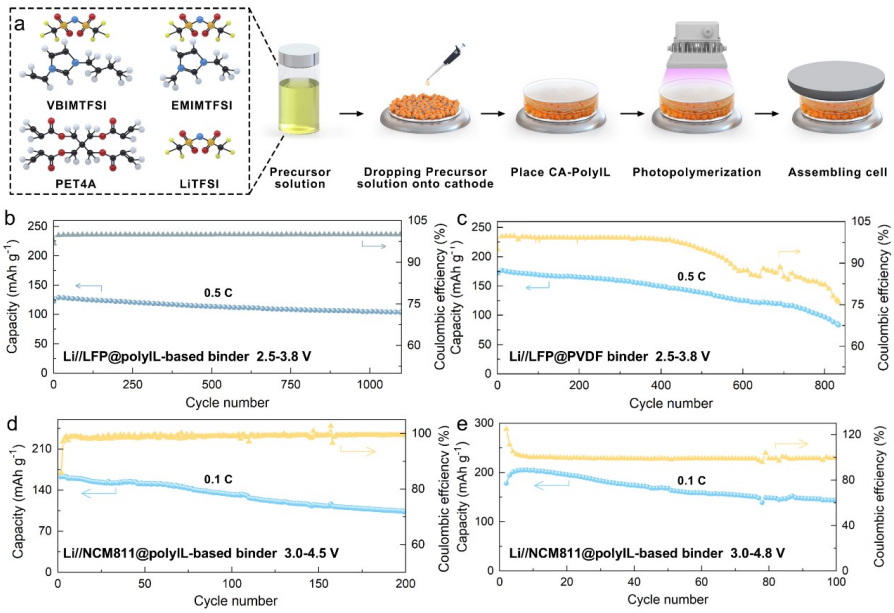

Figure 4-16. (a) Schematic illustration depicting the in-situ fabrication of LMB. Cycling stability of LMBs using LFP with (b) polyIL-based binder and (c) PVDF binder. Cycling stability of LMBs assembled with high-voltage NCM811 at (d) 3.0-4.5 V and (e) 3.0-4.8 V.

Table 4-1. Comparison of cut-off potentials for Li//NCM811 or Li//FFP cells with different cathode binders.

Electrolyte	Binder	Oxidation potential	Cell cathode	Cell operating potential	Ref.
1 M $LiPF_6$ in 1:1 EC:DEC (vol %) with 10 wt.% FEC and 1 wt.% VC	c-IPN	——	NCM811	4.4 V	50
1 M $LiPF_6$ in 1:1 EC:DMC	CPC	——	LFP	4.0 V	93

(vol %)					
1 M $LiPF_6$ in 1:1 EC:DMC (vol %)	P3	4.0 V	LFP	4.0 V	94
1 M $LiPF_6$ in 1:1 EC:PC (vol %) with ETPTA at 85:15 (w %)	1 M $LiPF_6$ in 1:1 EC:PC (vol %) with ETPTA at 85:15 (w %)	——	NCM811	4.4 V	95
GPE-G4	PDADMA-CFSO	5.1 V	NCM811	4.2 V	49
Li_6PS_5Cl	EMG	——	NCM811-1	3.7 V	96
1 M $LiPF_6$ in 3:7 EC:EMC (vol %)	PVDF	——	NCM811	4.3 V	97
1 M LiTFSI and LiDFOB in G4	PVDF	4.5 V	NCM811	4.5 V	98
1.2 M $LiPF_6$ in 4:1 DMC:FEC (vol %)	PVDF	——	NCM811-LLZO	4.3 V	99
0.5 M LiTFSI, 0.25 M $LiBF_4$, and 1 M $LiPF_6$ in 1:1 EC:DME (vol %) and DOL	PVDF	4.8 V	NCM811	4.3 V	100
PEO/LiTFSI/3DMoO_3	PVDF	——	NCM811	4.3 V (100)	101
polyIL-SPE	**PolyIL-based SPE**	**5.2 V**	**NCM811**	**4.8 V**	**This work**
PolyIL@CA-PolyIL SPE					

Fluoroethylene carbonate (FEC), vinylene carbonate (VC), ethylene carbonate (EC), dimethyl carbonate (DMC), propylene carbonate (PC), ethoxylated trimethylolpropane

triacrylate (ETPTA), poly(ethylene-co-methyl acrylate-co-glycidyl methacrylate) (EMG), $LiNi_{0.78}Co_{0.10}Mn_{0.12}O_2$ (NCM-1), tetraglyme (G4), lithium bis(trifluoromethanesulfonyl)imide (LiTFSI), lithium difluoro(oxalato)borate (LiDFOB), 1,3-dioxolane (DOL), lithium tetrafluoroborate salt ($LiBF_4$), lithium hexafluorophosphate ($LiPF_6$), poly(1-(4-vinylbenzyl)-2,3-dimethylimidazolium TFSI) (P3).

4.4.5 Sub-summary

This part developed a polyIL-based SPE by combining a polyIL-based material host with a modified CA-polyIL substrate. The CA-polyIL substrate improved the properties of the SPE, enhancing ionic conductivity (0.05 to 0.12 mS cm^{-1} at RT), t_{Li^+} (0.15 to 0.28), and mechanical strength (1.4 to 29.9 MPa). Replacing the PVDF binder with the polyIL-based material doubled the Li^+ diffusion rate within the model LFP cathode. Similar constituents in the cathode and SPE ensure their interfacial compatibility, leading to stable cycling of the Li//LFP cells for over 1100 cycles and allowing the Li//NCM811 cells to operate at high cut-off potentials of up to 4.5 V and even 4.8 V. This part of work represents a significant advancement in the exploration of polyIL-based materials for high-potential LMBs and underscores the crucial role of cathode-SPE compatibility in extending the cycle life of LMBs.

5. Conclusions and future work

5.1 Conclusions

This thesis was to develop polyIL-based SSEs with enhanced properties, including high ionic conductivity, a wide ESW, a high t_{Li^+}, and effective suppression of lithium dendrites growth for LMBs, enabling the assembled LMBs to be compatible with high-voltage cathodes while achieving a long cycle life. These advancements were achieved by optimizing the constituents of SSEs, refining their preparation methods, and exploring their applicability in the cathode as a bind. The key conclusions of this thesis are as follows:

Optimizing constituents in polyIL-based SSEs: IL additive, Li-salt, inorganic fillers, and polyIL-host are common constituents in polyIL-based SSEs. Among the IL additives, traditional ILs are identified as promising options due to their high ionic conductivity and wide ESW. In comparison, DES offers modest performance enhancements, while SIL is often utilized in liquid organic electrolytes. For the F-based Li-salts in the polyIL-based SSEs, the SEI characteristics, which influence lithium dendrite growth, are determined by the F-connecting bonds rather than the F atomic content. This conclusion is supported by AIMD simulations, which reveals that only the Li-salt molecules near the Li metal anode decompose to form LiF, while those farther away tend to bond with oxygen to form Li_2O. LiTFSI was identified as the most suitable choice, as it significantly improved the properties and performance of SSEs and LMBs while remaining cost-effective. For the filler in the polyIL-based SCEs, whether inert or active inorganic ones, there is always an optimal value to provide the highest ionic conductivity and the widest ESW. This is because inert inorganic fillers alter the crystallinity of the polymer host, while active fillers modify the Li^+ transport pathway.

Developing polyIL-based SSEs with desirable electrochemical properties: This thesis developed three types of polyIL-based SSEs, where the ionic conductivity, ESW, and t_{Li^+} gradually were improved, and the maximum cut-off potential, compatible with high-voltage cathodes, was also increased accordingly. Furthermore, the cycle life of the cells showed steady improvement.

Innovative methods for preparing polyIL-based SSEs and exploring their versatility: This thesis employed in-situ natural sedimentation methods for preparing the polyIL-based SSE, effectively reducing interfacial resistance between SSEs and

electrodes while simultaneously meeting the requirements of both the cathode and Li metal anode. As a result, the assembled LMBs have progressed from being paired with low-voltage $LiFePO_4$ (2.5-3.8 V) to high-voltage $LiMn_xFe_{1-x}PO_4$ (2.5-4.3 V). Additionally, a polyIL-based material was simultaneously employed as both an SPE host and a cathode binder, which was further combined with the in-situ polymerization, enhancing cathode-SSE interfacial compatibility and improving the LMB performance. The assembled Li//$LiFePO_4$ achieved over 1100 cycles, and the Li//$LiNi_{0.8}Co_{0.1}Mn_{0.1}O_4$ cell operated at a high cut-off potential of 4.8 V.

5.2 Future work

This doctoral thesis explored the effects of the constituents of SSEs for LMBs on the ionic conductivity, t_{Li^+}, and assembled battery performance. These explorations range from the development of promising individual constituents to the engineering of SSEs. However, most conclusions are based on experimental electrochemical results, leaving room for further validation and insight from a theoretical perspective.

From the perspective of ILs, the mechanism of ILs on enhancing properties of ionic conductivity, t_{Li^+}, and ESW remains unclear. A deeper understanding of the role of ILs in polyIL-based SSEs is crucial for advancing the development of 5-V class LMBs.

While this thesis primarily emphasizes the development of polyIL-based SSEs for high-temperature applications, the exploration of low or RT polyIL-based SSEs remains an important direction for future research.

6. References

1. Ostwald, W., Die wissenschaftliche elektrochemie der gegenwart und die technische der zukunft. **1894,** *15U* (1), 409.

2. Zhang, Q. L.; O'Brien, S. C.; Heath, J. R.; Liu, Y.; Curl, R. F.; Kroto, H. W.; Smalley, R. E., Reactivity of large carbon clusters: spheroidal carbon shells and their possible relevance to the formation and morphology of soot. *The Journal of Physical Chemistry*, **1986,** *90* (4), 525.

3. Shen, Y.; Zhang, Y.; Han, S.; Wang, J.; Peng, Z.; Chen, L., Unlocking the energy capabilities of lithium metal electrode with solid-state electrolytes. *Joule*, **2018,** *2* (9), 1674.

4. Dunn, B.; Kamath, H.; Tarascon, J. M., Electrical energy storage for the grid: A battery of choices. *Science*, **2011,** *334* (6058), 928.

5. Goodenough, J. B.; Park, K. S., The Li-ion rechargeable battery: A perspective. *Journal of the American Chemical Society*, **2013,** *135* (4), 1167.

6. Armand, M.; Tarascon, J. M., Building better batteries. *Nature*, **2008,** *451* (7179), 652.

7. Zhang, J.; Zhang, H.; Weng, S.; Li, R.; Lu, D.; Deng, T.; Zhang, S.; Lv, L.; Qi, J.; Xiao, X.; Fan, L.; Geng, S.; Wang, F.; Chen, L.; Noked, M.; Wang, X.; Fan, X., Multifunctional solvent molecule design enables high-voltage Li-ion batteries. *Nature Communications*, **2023,** *14* (1), 2211.

8. Su, H.; Chen, Z.; Li, M.; Bai, P.; Li, Y.; Ji, X.; Liu, Z.; Sun, J.; Ding, J.; Yang, M.; Yao, X.; Mao, C.; Xu, Y., Achieving practical high-energy-density lithium metal batteries by a dual-anion regulated electrolyte. *Advanced Materials*, **2023**, *35* (29), 2301171.

9. Ji, W.; Luo, B.; Wang, Q.; Yu, G.; Liu, Z.; Zhao, Z.; Zhao, R.; Wang, S.; Wang, X.; Zhang, B.; Zhang, J.; Hou, F.; Liang, J., Revealing the influence of surface microstructure on Li wettability and interfacial ionic transportation for garnet-type electrolytes. *Advanced Energy Materials*, **2023**, *13* (21), 2300165.

10. Zhou, Q.; Ma, J.; Dong, S.; Li, X.; Cui, G., Intermolecular chemistry in solid polymer electrolytes for high-energy-density lithium batteries. *Advanced Materials*, **2019,** *31* (50), 1902029.

11. Eshetu, G. G.; Judez, X.; Li, C.; Martinez-Ibañez, M.; Gracia, I.; Bondarchuk, O.; Carrasco, J.; Rodriguez-Martinez, L. M.; Zhang, H.; Armand, M., Ultrahigh

performance all solid-state lithium sulfur batteries: Salt anion's chemistry-induced anomalous synergistic effect. *Journal of the American Chemical Society*, **2018,** *140* (31), 9921.

12. Zhang, H.; Armand, M., History of solid polymer electrolyte-based solid-state lithium metal batteries: A personal account. *Israel Journal of Chemistry*, **2021,** *61* (1-2), 94.

13. Linert, W.; Camard, A.; Armand, M.; Michot, C., Anions of low Lewis basicity for ionic solid state electrolytes. *Coordination Chemistry Reviews*, **2002,** *226* (1), 137.

14. Barbosa, J. C.; Gonçalves, R.; Costa, C. M.; de Zea Bermudez, V.; Fidalgo-Marijuan, A.; Zhang, Q.; Lanceros-Méndez, S., Metal–organic frameworks and zeolite materials as active fillers for lithium-ion battery solid polymer electrolytes. *Materials Advances*, **2021,** *2* (12), 3790.

15. Jagadeesan, A.; Sasikumar, M.; Jeevani, R.; Therese, H. A.; Ananth, N.; Sivakumar, P., Fabrication of $BaTiO_3$ ceramic filler incorporated PVC-PEMA based blend nanocomposite gel polymer electrolytes for Li ion battery applications. *Journal of Materials Science: Materials in Electronics*, **2019,** *30* (18), 17181.

16. Yang, X.; Liu, J.; Pei, N.; Chen, Z.; Li, R.; Fu, L.; Zhang, P.; Zhao, J., The Critical Role of fillers in composite polymer electrolytes for lithium battery. *Nano-Micro Letters*, **2023,** *15* (1), 74.

17. Yao, M.; Ruan, Q.; Wang, Y.; Du, L.; Li, Q.; Xu, L.; Wang, R.; Zhang, H., A robust dual-polymer@inorganic networks composite polymer electrolyte toward ultra-long-life and high-voltage Li/Li-rich metal battery. *Advanced Functional Materials*, **2023,** *33* (18), 2213702.

18. Wu, P.; Zhou, W.; Su, X.; Li, J.; Su, M.; Zhou, X.; Sheldon, B. W.; Lu, W., Recent advances in conduction mechanisms, synthesis methods, and improvement strategies for $Li_{1+x}Al_xTi_{2-x}(PO_4)_3$ solid electrolyte for all-solid-state lithium batteries. *Advanced Energy Materials*, **2023,** *13* (4), 2203440.

19. Zheng, J.; Hu, Y. Y., New insights into the compositional dependence of Li-ion transport in polymer–ceramic composite electrolytes. *ACS Applied Materials & Interfaces*, **2018,** *10* (4), 4113.

20. Hirankumar, G.; Mehta, N., Effect of incorporation of different plasticizers on structural and ion transport properties of PVA-$LiClO_4$ based electrolytes. *Heliyon*, **2018,** *4* (12), e00992.

21. Chen, H.; Zheng, M.; Qian, S.; Ling, H. Y.; Wu, Z.; Liu, X.; Yan, C.; Zhang, S., Functional additives for solid polymer electrolytes in flexible and high-energy-density solid-state lithium-ion batteries. *Carbon Energy*, **2021,** *3* (6), 929.

22. Wang, X.; Salari, M.; Jiang, D. E.; Chapman Varela, J.; Anasori, B.; Wesolowski, D. J.; Dai, S.; Grinstaff, M. W.; Gogotsi, Y., Electrode material–ionic liquid coupling for electrochemical energy storage. *Nature Reviews Materials*, **2020,** *5* (11), 787.

23. Li, J.; Li, F.; Zhang, L.; Zhang, H.; Lassi, U.; Ji, X., Recent applications of ionic liquids in quasi-solid-state lithium metal batteries. *Green Chemical Engineering*, **2021,** *2* (3), 253.

24. Fenton, D. E.; Parker, J. M.; Wright, P. V., Complexes of alkali metal ions with poly(ethylene oxide). *Polymer*, **1973,** *14* (11), 589.

25. Fan, P.; Liu, H.; Marosz, V.; Samuels, N. T.; Suib, S. L.; Sun, L.; Liao, L., High performance composite polymer electrolytes for lithium-ion batteries. *Advanced Functional Materials*, **2021,** *31* (23), 2101380.

26. Yin, K.; Zhang, Z.; Li, X.; Yang, L.; Tachibana, K.; Hirano, S. I., Polymer electrolytes based on dicationic polymeric ionic liquids: application in lithium metal batteries. *Journal of Materials Chemistry A*, **2015,** *3* (1), 170.

27. Mecerreyes, D., Polymeric ionic liquids: Broadening the properties and applications of polyelectrolytes. *Progress in Polymer Science*, **2011,** *36* (12), 1629.

28. Eshetu, G. G.; Mecerreyes, D.; Forsyth, M.; Zhang, H.; Armand, M., Polymeric ionic liquids for lithium-based rechargeable batteries. *Molecular Systems Design & Engineering*, **2019,** *4* (2), 294.

29. Chen, H.; Choi, J. H.; Salas-de la Cruz, D.; Winey, K. I.; Elabd, Y. A., Polymerized ionic liquids: The effect of random copolymer composition on ion conduction. *Macromolecules*, **2009,** *42* (13), 4809.

30. Tang, J.; Tang, H.; Sun, W.; Radosz, M.; Shen, Y., Poly(ionic liquid)s as new materials for CO_2 absorption. *Chemical Communctions*, **2005,** *43* (22), 5477.

31. Hirao, M.; Ito, K.; Ohno, H., Preparation and polymerization of new organic molten salts; N-alkylimidazolium salt derivatives. *Electrochimica Acta*, **2000,** *45* (8), 1291.

32. Matsumoto, K.; Talukdar, B.; Endo, T., Synthesis and properties of methacrylate-based ionic networked polymers containing ionic liquids: comparison of ionic and nonionic networked polymers. *Polymer Bulletin*, **2011,** *66* (6), 771.

33. Appetecchi, G. B.; Kim, G. T.; Montanino, M.; Carewska, M.; Marcilla, R.; Mecerreyes, D.; De Meatza, I., Ternary polymer electrolytes containing pyrrolidinium-based polymeric ionic liquids for lithium batteries. *Journal of Power Sources*, **2010,** *195* (11), 3668.

34. Qian, W.; Texter, J.; Yan, F., Frontiers in poly(ionic liquid)s: syntheses and applications. *Chemical Society Reviews*, **2017,** *46* (4), 1124.

35. Hiroyuki, O.; Kaori, I., Room-temperature molten salt polymers as a matrix for fast ion conduction. *Chemistry Letters*, **1998,** *27* (8), 751.

36. Ohno, H., Molten salt type polymer electrolytes. *Electrochimica Acta*, **2001,** *46* (10), 1407.

37. Vygodskii, Y. S.; Mel'nik, O. A.; Shaplov, A. S.; Lozinskaya, E. I.; Malyshkina, I. A.; Gavrilova, N. D., Synthesis and ionic conductivity of polymer ionic liquids. *Polymer Science Series A*, **2007,** *49* (3), 256.

38. Pont, A. L.; Marcilla, R.; De Meatza, I.; Grande, H.; Mecerreyes, D., Pyrrolidinium-based polymeric ionic liquids as mechanically and electrochemically stable polymer electrolytes. *Journal of Power Sources*, **2009,** *188* (2), 558.

39. Nishimura, N.; Ohno, H., 15th anniversary of polymerised ionic liquids. *Polymer*, **2014,** *55* (16), 3289.

40. Zhang, P.; Li, M.; Yang, B.; Fang, Y.; Jiang, X.; Veith, G. M.; Sun, X. G.; Dai, S., Polymerized ionic networks with high charge density: Quasi-solid electrolytes in lithium-metal batteries. *Advanced Materials*, **2015,** *27* (48), 8088.

41. Frenzel, F.; Folikumah, M. Y.; Schulz, M.; Anton, A. M.; Binder, W. H.; Kremer, F., Molecular dynamics and charge transport in polymeric polyisobutylene-based ionic liquids. *Macromolecules*, **2016,** *49* (7), 2868.

42. Mogurampelly, S.; Keith, J. R.; Ganesan, V., Mechanisms Underlying ion transport in polymerized ionic liquids. *Journal of the American Chemical Society*, **2017,** *139* (28), 9511.

43. Wang, X.; Chen, F.; Girard, G. M. A.; Zhu, H.; MacFarlane, D. R.; Mecerreyes, D.; Armand, M.; Howlett, P. C.; Forsyth, M., Poly(Ionic Liquid)s-in-salt electrolytes with co-coordination-assisted lithium-ion transport for safe batteries. *Joule*, **2019,** *3* (11), 2687.

44. Girard, G. M. A.; Wang, X.; Yunis, R.; Howlett, P. C.; Forsyth, M., Stable performance of an all-solid-state Li metal cell coupled with a high-voltage NCA

cathode and ultra-high lithium content poly(ionic liquid)s-based polymer electrolyte. *Journal of Solid State Electrochemistry*, **2020,** *24* (10), 2479.

45. Fu, C.; Homann, G.; Grissa, R.; Rentsch, D.; Zhao, W.; Gouveia, T.; Falgayrat, A.; Lin, R.; Fantini, S.; Battaglia, C., A polymerized-ionic-liquid-based polymer electrolyte with high oxidative stability for 4 and 5 V class solid-state lithium metal batteries. *Advanced Energy Materials*, **2022,** *12* (27), 2200412.

46. Wang, X.; Girard, G. M. A.; Zhu, H.; Yunis, R.; MacFarlane, D. R.; Mecerreyes, D.; Bhattacharyya, A. J.; Howlett, P. C.; Forsyth, M., Poly(ionic liquid)s/electrospun nanofiber composite polymer electrolytes for high energy density and safe Li metal batteries. *ACS Applied Energy Materials*, **2019,** *2* (9), 6237.

47. Li, Y.; Sun, Z.; Shi, L.; Lu, S.; Sun, Z.; Shi, Y.; Wu, H.; Zhang, Y.; Ding, S., Poly(ionic liquid)-polyethylene oxide semi-interpenetrating polymer network solid electrolyte for safe lithium metal batteries. *Chemical Engineering Journal*, **2019,** *375*, 121925.

48. Qin, T.; Yang, H.; Li, Q.; Yu, X.; Li, H., Design of functional binders for high-specific-energy lithium-ion batteries: from molecular structure to electrode properties. *Industrial Chemistry & Materials*, **2024,** *2* (2), 191.

49. Vauthier, S.; Alvarez-Tirado, M.; Guzmán-González, G.; Tomé, L. C.; Cotte, S.; Castro, L.; Guéguen, A.; Mecerreyes, D.; Casado, N., High-performance pyrrolidinium-based poly(ionic liquid) binders for Li-ion and Li-air batteries. *Materials Today Chemistry*, **2023,** *27*, 101293.

50. Kim, J. H.; Lee, K. M.; Kim, J. W.; Kweon, S. H.; Moon, H. S.; Yim, T.; Kwak, S. K.; Lee, S. Y., Regulating electrostatic phenomena by cationic polymer binder for scalable high-areal-capacity Li battery electrodes. *Nature Communications*, **2023,** *14* (1), 5721.

51. Song, X.; Zhang, H.; Jiang, D.; Yang, L.; Zhang, J.; Yao, M.; Ji, X.; Wang, G.; Zhang, S., Enhanced transport and favorable distribution of Li-ion in a poly(ionic liquid) based electrolyte facilitated by $Li_{1.3}Al_{0.3}Ti_{1.7}(PO_4)_3$ nanoparticles for highly-safe lithium metal batteries. *Electrochimica Acta*, **2021,** *368*, 137581.

52. Li, M.; Yang, B.; Wang, L.; Zhang, Y.; Zhang, Z.; Fang, S.; Zhang, Z., New polymerized ionic liquid (PIL) gel electrolyte membranes based on tetraalkylammonium cations for lithium ion batteries. *Journal of Membrane Science*, **2013,** *447*, 222.

53. Li, M.; Wang, L.; Yang, B.; Du, T.; Zhang, Y., Facile preparation of polymer electrolytes based on the polymerized ionic liquid poly((4-vinylbenzyl)trimethylammonium bis(trifluoromethanesulfonylimide)) for lithium secondary batteries. *Electrochimica Acta*, **2014,** *123*, 296.

54. Song, X.; Wang, C.; Chen, J.; Xin, S.; Yuan, D.; Wang, Y.; Dong, K.; Yang, L.; Wang, G.; Zhang, H.; Zhang, S., Unraveling the synergistic coupling mechanism of Li^+ transport in an "ionogel-in-ceramic" hybrid solid electrolyte for rechargeable lithium metal battery. *Advanced Functional Materials*, **2022,** *32* (10), 2108706.

55. Li, S.; Zhang, Z.; Yang, K.; Yang, L., Polymeric ionic liquid-poly(ethylene glycol) composite polymer electrolytes for high-temperature lithium-ion batteries. *ChemElectroChem*, **2018,** *5* (2), 328.

56. Li, M.; Dong, S.; Fang, S.; Yang, L.; Hirano, S. I.; Hu, J.; Huang, X., Polymeric ionic liquid membranes as electrolytes for lithium battery applications. *Journal of Applied Electrochemistry*, **2012,** *42* (10), 851.

57. Li, M.; Yang, L.; Fang, S.; Dong, S.; Hirano, S. I.; Tachibana, K., Polymerized ionic liquids with guanidinium cations as host for gel polymer electrolytes in lithium metal batteries. *Polymer International*, **2012,** *61* (2), 259.

58. Safa, M.; Chamaani, A.; Chawla, N.; El-Zahab, B., Polymeric ionic liquid gel electrolyte for room temperature lithium battery applications. *Electrochimica Acta*, **2016,** *213*, 587.

59. Wang, A.; Xu, H.; Liu, X.; Gao, R.; Wang, S.; Zhou, Q.; Chen, J.; Liu, X.; Zhang, L., The synthesis of a hyperbranched star polymeric ionic liquid and its application in a polymer electrolyte. *Polymer Chemistry*, **2017,** *8* (20), 3177.

60. Wang, Z.; Zhou, H.; Meng, C.; Xiong, W.; Cai, Y.; Hu, P.; Pang, H.; Yuan, A., Enhancing ion transport: Function of ionic liquid decorated MOFs in polymer electrolytes for all-solid-state lithium batteries. *ACS Applied Energy Materials*, **2020,** *3* (5), 4265.

61. Jaumaux, P.; Liu, Q.; Zhou, D.; Xu, X.; Wang, T.; Wang, Y.; Kang, F.; Li, B.; Wang, G., Deep-eutectic-solvent-based self-healing polymer electrolyte for safe and long-Life lithium-metal batteries. *Angewandte Chemie International Edition*, **2020,** *59* (23), 9134.

62. Yu, L.; Guo, S.; Lu, Y.; Li, Y.; Lan, X.; Wu, D.; Li, R.; Wu, S.; Hu, X., Highly tough, Li-metal compatible organic–inorganic double-network solvate ionogel. *Advanced Energy Materials*, **2019,** *9* (22), 1900257.

63. Zhang, Z.; Zhang, L.; Liu, Y.; Wang, H.; Yu, C.; Zeng, H.; Wang, L. M.; Xu, B., Interface-engineered $Li_7La_3Zr_2O_{12}$-based garnet solid electrolytes with suppressed Li-dendrite formation and enhanced electrochemical performance. *ChemSusChem*, **2018,** *11* (21), 3774.

64. Matsuura, S.; Shibata, M.; Han, J.; Fujii, K., Polymer gel electrolyte prepared by "salting-in" poly(ethylene glycol) into a phosphonium-based ionic liquid with a lithium salt. *ACS Applied Polymer Materials*, **2020,** *2* (3), 1276.

65. Tian, X.; Yi, Y.; Yang, P.; Liu, P.; Qu, L.; Li, M.; Hu, Y. S.; Yang, B., High-charge density polymerized ionic networks boosting high ionic conductivity as quasi-solid electrolytes for high-voltage batteries. *ACS Applied Materials & Interfaces*, **2019,** *11* (4), 4001.

66. Clarke-Hannaford, J.; Breedon, M.; Rüther, T.; Spencer, M. J. S., Stability of boronium cation-based ionic liquid electrolytes on the Li metal anode surface. *ACS Applied Energy Materials*, **2020,** *3* (6), 5497.

67. Zhao, Q.; Stalin, S.; Zhao, C. Z.; Archer, L. A., Designing solid-state electrolytes for safe, energy-dense batteries. *Nature Reviews Materials*, **2020,** *5* (3), 229.

68. Luo, S.; Zhang, Q.; Zhu, L.; Lin, H.; Kazanowska, B. A.; Doherty, C. M.; Hill, A. J.; Gao, P.; Guo, R., Highly selective and permeable microporous polymer membranes for hydrogen purification and CO_2 removal from natural gas. *Chemistry of Materials*, **2018,** *30* (15), 5322.

69. Li, M.; Zhu, W.; Zhang, P.; Chao, Y.; He, Q.; Yang, B.; Li, H.; Borisevich, A.; Dai, S., Graphene-analogues boron nitride nanosheets confining ionic liquids: A high-performance quasi-liquid solid electrolyte. *Small*, **2016,** *12* (26), 3535.

70. Cheng, Y.; Zhang, X.; Yin, C.; Zhang, J.; Yu, J.; Zhang, J., Immobilization of ionic liquids with a new cellulose ester containing imidazolium cation for high-performance CO_2 separation membranes. *Macromolecular Rapid Communications*, **2021,** *42* (3), 2000494.

71. Grimme, S.; Antony, J.; Ehrlich, S.; Krieg, H., A consistent and accurate ab initio parametrization of density functional dispersion correction (DFT-D) for the 94 elements H-Pu. *The Journal of Chemical Physics*, **2010,** *132* (15), 154104.

72. Grimme, S.; Ehrlich, S.; Goerigk, L., Effect of the damping function in dispersion corrected density functional theory. *Journal of Computational Chemistry*, **2011,** *32* (7), 1456.

73. Marenich, A. V.; Cramer, C. J.; Truhlar, D. G., Universal solvation model based on solute electron density and on a continuum model of the solvent defined by the bulk dielectric constant and atomic surface tensions. *The Journal of Physical Chemistry B* **2009,** *113* (18), 6378.

74. Deng, C.; Chen, N.; Hou, C.; Liu, H.; Zhou, Z.; Chen, R., Enhancing interfacial contact in solid-state batteries with a gradient composite solid electrolyte. *Small*, **2021,** *17* (18), 2006578.

75. Kohn, W.; Sham, L. J., Self-consistent equations including exchange and correlation effects. *Physical Review*, **1965,** *140* (4A), A1133.

76. Monkhorst, H. J.; Pack, J. D., Special points for Brillouin-zone integrations. *Physical Review B*, **1976,** *13* (12), 5188.

77. Rappe, A. K.; Casewit, C. J.; Colwell, K. S.; Goddard, W. A., III; Skiff, W. M., UFF, a full periodic table force field for molecular mechanics and molecular dynamics simulations. *Journal of the American Chemical Society*, **1992,** *114* (25), 10024.

78. Nosé, S., A unified formulation of the constant temperature molecular dynamics methods. *The Journal of Chemical Physics*, **1984,** *81* (1), 511.

79. McKenzie, I.; Harada, M.; Kiefl, R. F.; Levy, C. D. P.; MacFarlane, W. A.; Morris, G. D.; Ogata, S. I.; Pearson, M. R.; Sugiyama, J., β-NMR measurements of lithium ion transport in thin films of pure and lithium-salt-doped poly(ethylene oxide). *Journal of the American Chemical Society*, **2014,** *136* (22), 7833.

80. Zhou, M. Y.; Ding, X. Q.; Ding, J. F.; Hou, L. P.; Shi, P.; Xie, J.; Li, B. Q.; Huang, J. Q.; Zhang, X. Q.; Zhang, Q., Quantifying the apparent electron transfer number of electrolyte decomposition reactions in anode-free batteries. *Joule*, **2022,** *6* (9), 2122.

81. Budi, A.; Basile, A.; Opletal, G.; Hollenkamp, A. F.; Best, A. S.; Rees, R. J.; Bhatt, A. I.; O'Mullane, A. P.; Russo, S. P., Study of the initial stage of solid electrolyte interphase formation upon chemical reaction of lithium metal and n-methyl-n-propyl-pyrrolidinium-bis(Fluorosulfonyl)imide. *The Journal of Physical Chemistry C*, **2012,** *116* (37), 19789.

82. Tian, Z.; Hou, L.; Feng, D.; Jiao, Y.; Wu, P., Modulating the coordination environment of lithium bonds for high performance polymer electrolyte batteries. *ACS Nano*, **2023,** *17* (4), 3786.

83. Hu, S.; Lozada-Hidalgo, M.; Wang, F. C.; Mishchenko, A.; Schedin, F.; Nair, R. R.; Hill, E. W.; Boukhvalov, D. W.; Katsnelson, M. I.; Dryfe, R. A. W.; Grigorieva, I. V.;

Wu, H. A.; Geim, A. K., Proton transport through one-atom-thick crystals. *Nature*, **2014,** *516* (7530), 227.

84. Zhang, X.; Liu, T.; Zhang, S.; Huang, X.; Xu, B.; Lin, Y.; Xu, B.; Li, L.; Nan, C. W.; Shen, Y., Synergistic coupling between $Li_{6.75}La_3Zr_{1.75}Ta_{0.25}O_{12}$ and poly(vinylidene fluoride) induces high ionic conductivity, mechanical strength, and thermal stability of solid composite electrolytes. *Journal of the American Chemical Society*, **2017,** *139* (39), 13779.

85. Zhang, J.; Zang, X.; Wen, H.; Dong, T.; Chai, J.; Li, Y.; Chen, B.; Zhao, J.; Dong, S.; Ma, J.; Yue, L.; Liu, Z.; Guo, X.; Cui, G.; Chen, L., High-voltage and free-standing poly(propylene carbonate)/$Li_{6.75}La_3Zr_{1.75}Ta_{0.25}O_{12}$ composite solid electrolyte for wide temperature range and flexible solid lithium ion battery. *Journal of Materials Chemistry A*, **2017,** *5* (10), 4940.

86. Chen, L.; Fu, J.; Lu, Q.; Shi, L.; Li, M.; Dong, L.; Xu, Y.; Jia, R., Cross-linked polymeric ionic liquids ion gel electrolytes by in situ radical polymerization. *Chemical Engineering Journal*, **2019,** *378*, 122245.

87. Liang, H. P.; Chen, Z.; Dong, X.; Zinkevich, T.; Indris, S.; Passerini, S.; Bresser, D., Photo-cross-linked single-ion conducting polymer electrolyte for lithium-metal batteries. *Macromolecular Rapid Communications*, **2022,** *43* (12), 2100820.

88. Zhang, H.; Liao, X.; Guan, Y.; Xiang, Y.; Li, M.; Zhang, W.; Zhu, X.; Ming, H.; Lu, L.; Qiu, J.; Huang, Y.; Cao, G.; Yang, Y.; Mai, L.; Zhao, Y.; Zhang, H., Lithiophilic-lithiophobic gradient interfacial layer for a highly stable lithium metal anode. *Nature Communications*, **2018,** *9* (1), 3729.

89. Wang, C.; Liu, H.; Liang, Y.; Li, D.; Zhao, X.; Chen, J.; Huang, W.; Gao, L.; Fan, L. Z., Molecular-level designed polymer electrolyte for high-voltage lithium–metal solid-state batteries. *Advanced Functional Mateials*, **2023,** *33* (3), 2209828.

90. Zhang, J.; Zhao, J.; Yue, L.; Wang, Q.; Chai, J.; Liu, Z.; Zhou, X.; Li, H.; Guo, Y.; Cui, G.; Chen, L., Safety-reinforced poly(propylene carbonate)-based all-solid-state polymer electrolyte for ambient-temperature solid polymer lithium batteries. *Advanced Energy Materials*, **2015,** *5* (24), 1501082.

91. He, Y.; Wang, C.; Zou, P.; Lin, R.; Hu, E.; Xin, H. L., Anion-tethered single lithium-ion conducting polyelectrolytes through UV-induced free radical polymerization for improved morphological stability of lithium metal anodes. *Angewandte Chemie International Edition*, **2023,** *62* (38), e202308309.

92. Liu, Y.; Zou, H.; Huang, Z.; Wen, Q.; Lai, J.; Zhang, Y.; Li, J.; Ding, K.; Wang, J.; Lan, Y. Q.; Zheng, Q., In situ polymerization of 1,3-dioxane as a highly compatible polymer electrolyte to enable the stable operation of 4.5 V Li-metal batteries. *Energy & Environmental Science*, **2023,** *16* (12), 6110.

93. Pace, G. T.; Le, M. L.; Clément, R. J.; Segalman, R. A., A coacervate-based mixed-conducting binder for high-power, high-energy batteries. *ACS Energy Letters* **2023,** *8* (6), 2781.

94. Lee, J. S.; Sakaushi, K.; Antonietti, M.; Yuan, J., Poly(ionic liquid) binders as Li^+ conducting mediators for enhanced electrochemical performance. *RSC Advances* **2015,** *5* (104), 85517.

95. Kim, J. H.; Kim, J. M.; Cho, S. K.; Kim, N. Y.; Lee, S. Y., Redox-homogeneous, gel electrolyte-embedded high-mass-loading cathodes for high-energy lithium metal batteries. *Nature Communications* **2022,** *13* (1), 2541.

96. Hong, S. B.; Jang, Y. R.; Kim, H.; Jung, Y. C.; Shin, G.; Hah, H. J.; Cho, W.; Sun, Y. K.; Kim, D. W., Wet-processable binder in composite cathode for high energy density all-solid-state lithium batteries. *Advanced Energy Materials* **2024***, 14* (35), 2400802.

97. Karanth, P.; Weijers, M.; Ombrini, P.; Ripepi, D.; Ooms, F.; Mulder, F. M., A phase inversion strategy for low-tortuosity and ultrahigh-mass-loading nickel-rich layered oxide electrodes. *Cell Reports Physical Science* **2024,** *5* (6), 101972.

98. Xia, D.; Tao, L.; Hou, D.; Hu, A.; Sainio, S.; Nordlund, D.; Sun, C.; Xiao, X.; Li, L.; Huang, H.; Lin, F., A green, fire-retarding ether solvent for sustainable high-voltage Li-ion batteries at standard salt concentration. *Advanced Energy Materials* **2024***, 14* (38), 2400773.

99. Bunyanidhi, P.; Phattharasupakun, N.; Tomon, C.; Duangdangchote, S.; Kidkhunthod, P.; Sawangphruk, M., Mechanofusing garnet solid electrolyte on the surface of Ni-rich layered oxide cathode towards high-rate capability of cylindrical Li-ion battery cells. *Journal of Power Sources* **2022**, *549*, 232043.

100. Liu, Q.; Sun, Y.; Wang, S.; An, Q.; Duan, L.; Zhao, G.; Wang, C.; Doyle-Davis, K.; Guo, H.; Sun, X., Highly adaptable SEI/CEI interfacial layers enabling remarkable performance of high-nickel solid-state batteries. *Materials Today* **2023**, *64*, 21-30.

101. Wang, X.; Huang, S.; Guo, K.; Min, Y.; Xu, Q., Directed and continuous interfacial channels for optimized ion transport in solid-state electrolytes. *Advanced Functional Materials* **2022,** *32* (49), 2206976.

Department of Engineering Science and Mathematics
Division of Energy Science

ISSN 1402-1544
ISBN 978-91-8048-728-3 (print)
ISBN 978-91-8048-729-0 (pdf)

Luleå University of Technology 2025

LULEÅ
UNIVERSITY
OF TECHNOLOGY